fhwedel

UNIVERSITY OF APPLIED SCIENCES

IT-Engineering

Impact of ocean-generated microseism on the European X-ray Free Electron Laser

Supervisor:

Prof. Dr. Carsten Burmeister

Fachhochschule Wedel gGmbH

Feldstraße 143

22880 Wedel

carsten.burmeister@fh-wedel.de

Author:

Erik Genthe

Deutsches Elektronen-Synchrotron DESY

Notkestraße 85

22607 Hamburg

erik.genthe@desy.de

Supervisor:

Dr. Holger Schlarb

Deutsches Elektronen-Synchrotron DESY

Notkestraße 85

22607 Hamburg

holger.schlarb@desy.de

Abstract

In this thesis, it is shown that ocean-generated microseism significantly impacts the synchronisation performance of the European X-ray free-electron laser (XFEL), which is based on a high-energy linear accelerator. Using superconducting technology, it generates hard X-ray pulses at megahertz frequencies. Arrival time stability refers to the precision and consistency of the timing of the X-ray pulses, ensuring that they arrive at the target with minimal variation in their temporal alignment. Ocean-generated microseism is low-frequency seismic noise caused by the interaction of ocean waves with the seabed. Distributed acoustic sensing (DAS) is a technology that turns optical fibres into a sensor array for monitoring acoustic signals along their length. By measuring tiny changes in light reflection caused by acoustic disturbances, DAS can provide real-time information about vibrations over long distances.

Notably, the bunch arrival time monitors (BAM) show noise between $0.05\,\mathrm{Hz}$ and $0.5\,\mathrm{Hz}$, which has a significant impact on the arrival time stability at European XFEL. The impact can be more than $25\,\mathrm{fs}$ peak-to-peak. By correlating European XFEL bunch arrival time data with seismic DAS measurements, it is shown that the noise is of seismic origin. Next, both primary and secondary ocean-generated microseism were identified using seismometers and a numerical ocean wave model. Whereas secondary microseism has a strong impact on the bunch arrival time, primary microseism has no notable effect. This is attributed not only to the smaller amplitudes of secondary microseism but also to the fact that primary microseism has a higher Love wave to Rayleigh wave ratio. The effect on the bunch arrival time is caused by Rayleigh waves, while Love waves have a negligible influence on the bunch arrival time. In the presented cases, the noise originates from the North Atlantic and/or the North Sea. The amplitude of the noise depends on the weather conditions in the North Sea and the North Atlantic and is generally much stronger in winter. In conclusion, this work shows that ocean-generated microseism is a significant bottleneck that must be addressed to achieve femtosecond bunch arrival time stability.

Contents

1 Introduction

The European X-ray free-electron LASER (XFEL) generates bursts of up to 2700 ultra-short X-ray flashes every 100 ms, with a brilliance that is a billion times greater than conventional X-ray sources. This facility opens up unprecedented research opportunities for scientists and industrial users (Altarelli et al. 2006). The European XFEL is located in underground tunnels stretching more than 3 km from the DESY site in Hamburg. The facility, which is part of a collaboration among twelve countries, is operated by European XFEL GmbH. The European XFEL accelerates electrons to nearly the speed of light and then sends them through undulators. Undulators are alternating magnets that force the electrons to oscillate, resulting in the emission of exceptionally short and intense X-ray flashes. This process is called self-amplified spontaneous emission (SASE), creating flashes with LASER properties (Geloni et al. 2010). Meaning that the light is polarised and has a narrow frequency band (monochromatic), high phase coherence, and high directionality. These LASER X-ray flashes enable unique experiments such as hologram recording. Although FELs of similar size exist in Japan and the USA, the European XFEL is unique because of its superconducting accelerator. This allows for the creation of bunches at a much faster rate, which is a decisive advantage for a wide range of experiments (DESY 2023).

The European XFEL is an important tool for conducting pump-probe experiments, which are used to study ultrafast phenomena such as atomic motion. An ultrashort LASER pulse excites the sample, followed by another LASER pulse that captures the response of the sample. Combining several measurements can provide insights into fast molecular processes, such as biological or chemical reactions that take place within a few femtoseconds (Palmer et al. 2019). As the demand for higher spatial and temporal resolution in these experiments increases, there is a growing need to improve the temporal stability of the X-ray flashes (Bock 2013).

The European XFEL generates bursts of intense X-ray flashes. Bursts, also called bunch-trains, are created at a rate of 10 Hz. Within a burst, up to 2700 bunches of electrons can be generated at a rate of 4.5 MHz, resulting in a maximum bunch-train duration of 600 µs (Czwalinna et al. 2021, Palmer et al. 2019). Ensuring that these bunches arrive at exactly 4.5 MHz with low jitter within a bunch train is called bunch arrival time stability (Schulz et al. 2019), which is a critical property of the XFEL. The present work aims to investigate potential improvements of this property. Accelerator synchronisation, such as bunch arrival time stability, has enabled remarkable progress over the past few decades. In 2000, synchronisation reached an accuracy of 1 ps. By 2010, this accuracy was improved to 100 fs femtoseconds and by 2020, synchronisation reached 10 fs (Schulz et al. 2019). Projecting this trend into the future, the next goal is to reach a level of 1 fs by 2030.

Five main areas for reducing bunch arrival time jitter have been identified (H. Schlarb 2023). The first is to improve the existing electron beam stabilisation. Accordingly, a new generation of bunch arrival time monitors (BAM) is under development. Second, the pump-LASER system introduces jitter, which can be compensated using LASER-pulse arrival time monitors (LAM) and fast feedback mechanisms (Czwalinna et al. 2021). Third, drifts occur in the optical reference system. Fourth, drifts that are caused by tidal effects. Fifth, a prominent noise peak is often observed in the 0.05 to 0.5 Hz frequency band. This disturbance has varying intensity and the frequency spectrum varies within the 0.05 to 0.5 Hz band. Similar characteristics have been observed in ocean-generated microseism (Longuet-Higgins 1950, Becker et al. 2020, Ardhuin et al. 2015). This thesis aims to investigate this noise band and determine its relation to ocean-generated microseism to gain a deeper understanding of the mechanism and explore ways of reducing the impact of ocean-generated microseism on experiments at the European XFEL, which is necessary to reach the 1 fs goal.

2 Background

This chapter provides an explanation of seismic waves, ocean-generated microseism, distributed acoustic sensing (DAS), the European XFEL, its BAMs, and the dCache storage system. Starting with basic theory, the chapter explains the theory of elastic wave propagation and introduces the four different types of waves that propagate in the Earth's crust. Moving on to known information on ocean-generated microseism. This is followed by a discussion of DAS, explaining its operating principles and its unique ability to turn an optical fibre into an array of virtual sensors for seismic monitoring. Next, the chapter examines the European XFEL, a free-electron laser, that is a collaborative effort among European countries to establish a state-of-the-art facility for X-ray research. This is followed by an explanation of the European XFEL's BAMs. These monitors play a crucial role in stabilising the arrival time of electron bunches, offering few-femtosecond resolution and serving as an indispensable component for a wide range of experiments where precise timing is paramount. Finally, the chapter introduces dCache, a high-performance distributed storage system that is essential for efficiently managing and storing the vast amounts of data generated by experiments and research activities. Overall, this chapter sets the stage for understanding the context of the following sections.

2.1 Seismic waves

There are two categories of waves to be expected in solid materials. Body waves, which propagate through solid volumes and surface waves, which propagate along free surfaces. These include compressional and shear waves (Figure 2.1). Because compressional waves travel faster than shear waves and arrive first, they are often called primary or P waves, whereas the later-arriving shear waves are called secondary or S waves.

However, when free surfaces exist in a medium, there can be two types of surface waves that can propagate along the Earth's surface: Rayleigh waves and Love waves. Love waves are purely horizontal motions perpendicular to the direction of propagation, whereas Rayleigh waves contain both vertical and radial motions. They differ from body waves in many aspects: their velocities are strongly frequency dependent, they generally travel more slowly, their amplitude is smaller, and decays less with distance. After large earthquakes, Surface waves are generally the strongest arrivals recorded at far distances and can be observed for many hours, during which time they circle the Earth several times (Anderson et al. 2007). Surface waves and normal modes are generally observed with periods longer than about 10 s, in contrast to the much shorter periods seen in many body wave observations. Furthermore, Rayleigh waves are generally radially polarised and exist in any free surface, whereas Love waves are transversely polarised and require

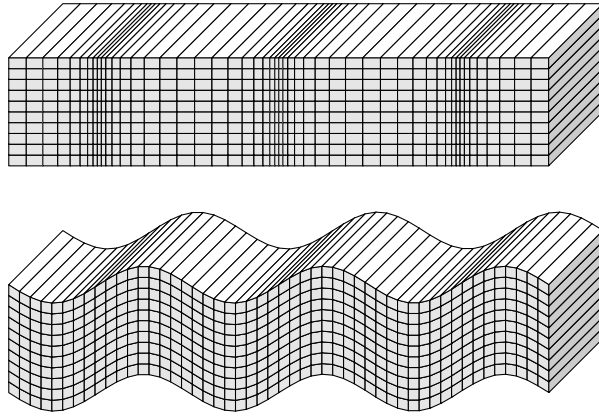an increase in velocity with depth in the medium ([Shearer 2019](#)).

Figure 2.1: Displacements resulting from a harmonic plane P-wave (top) and S-wave
(bottom) propagating horizontally across the page. The propagation of the
S-wave is a pure shear with no change in volume, whereas the P-wave
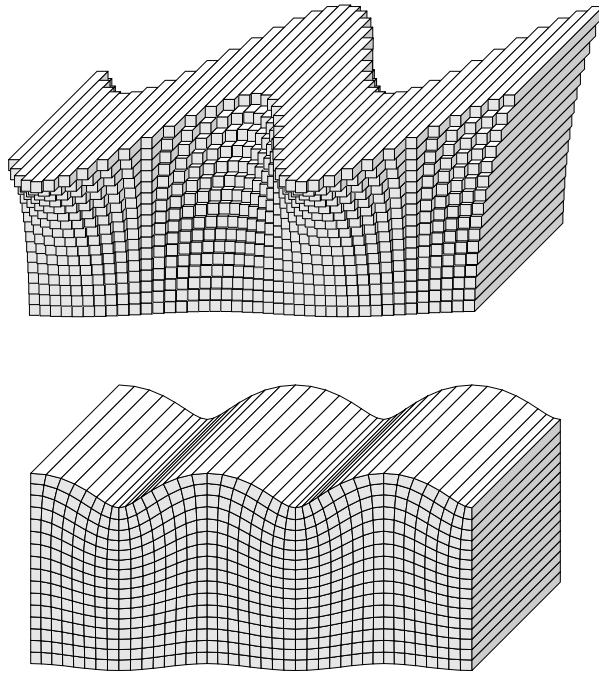involves both volume change and shear of the material. ([Shearer 2019](#))

Figure 2.2: Fundamental displacements of Love (top) and Rayleigh (bottom) surface
waves propagating horizontally across the page. Love waves are purely
horizontal motions perpendicular to the direction of propagation, whereas
Rayleigh waves contain both vertical and radial motions. In both cases, the
amplitude decreases with depth. ([Shearer 2019](#))

2.2 Ocean-generated Microseism

Even in the absence of earthquakes, there is continuous seismic noise, which is called microseism. Noise levels vary considerably at different locations and frequencies. In many scenarios, there is a significant peak between frequencies of 0.125 Hz to 0.2 Hz, dominating the frequency band below 1 Hz (Figure 2.3). This is strongest along the coast and is weaker near the centre of continents, suggesting that it is generated in the oceans. However, since the typical frequency of water waves in the ocean is about half the frequency of the main microseismic peak, the physical mechanism that generates these waves has not been understood for many years (Shearer 2019). The main peak in the microseism frequency band results from standing waves generated in the ocean by the superposition of ocean waves with different directions, which is referred to as secondary microseism (Longuet-Higgins 1950). Source regions of secondary microseism are often observed near the coast, due to the reflection of incoming ocean waves at the shore, and less frequently in open water locations.
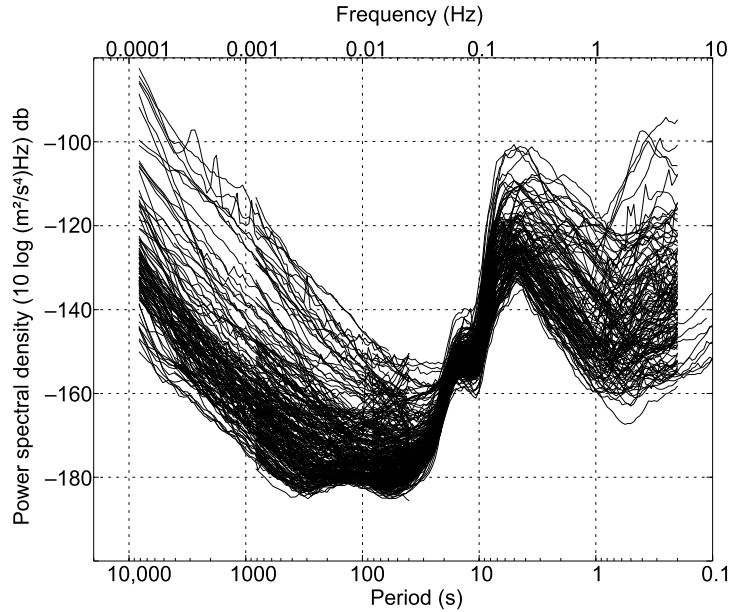

Figure 2.3: Measured vertical acceleration spectra of individual seismic stations worldwide, during periods without earthquakes. There is a prominent microseism peak between 0.12 Hz and 0.2 Hz, with a weaker peak around 0.07 Hz. The noise levels are significantly lower in the range of 0.005 Hz to 0.05 Hz. (Shearer 2019, Astiz 1997)

In contrast, primary microseism has the same frequency as the ocean waves that cause it and is generated by the contact of ocean waves along a rising seabed (Ardhuin et al. 2015). Consequently, primary microseism is also typically generated near the coast or in shallow water regions (Nishida et al. 2008). The amplitudes of primary microseism are usually orders of magnitude smaller than those of secondary microseism (Shearer 2019),

but due to the long wavelengths of primary microseism and the resulting low attenuation with distance, it can also be recorded globally.

At the seismic station on Helgoland primary and secondary microseism can be observed with a strong correlation to the local wave heights and frequencies. This microseism, which is most prominent in proximity to coastlines, is therefore called local microseism (Becker et al. 2020). While the local secondary microseism is usually very strong and easy to identify, local primary microseism is sometimes overlaid by microseism from other locations like the North Atlantic. The observed local primary microseism was measured with a higher horizontal-to-vertical ratio than the secondary microseism, which indicates a low contribution of Rayleigh waves (Becker et al. 2020). Local secondary microseism is particularly prominent in the 0.3 Hz to 1.0 Hz range (Figure 2.4) near the coast, and decays rapidly with distance (Chen et al. 2011).
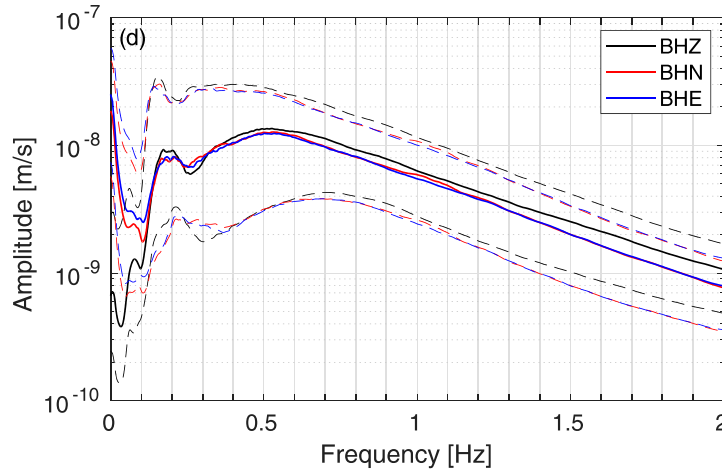

Figure 2.4: Seismometer average spectral amplitudes of the vertical, north, and east components of the HLG station on Helgoland, obtained at 2 h intervals from 2004 to 2019. Comparison of median, 10th, and 90th percentiles of the three components. The Peaks, observable in the vertical component below 0.1 Hz are primary microseism. At 0.17 Hz is secondary microseism and at 0.5 Hz is local microseism. (Becker et al. 2020)

The frequency of ocean waves depends on a number of factors. The strength of the wind is an important factor: Stronger winds, especially long periods of strong winds result in a lower frequency of ocean waves. Ocean wave frequency is also reduced by the size of the uninterrupted ocean surface, which allows the wind to travel long distances unhindered (Bretschneider 1959). In summary, smaller seas such as the North Sea are expected to have higher ocean wave frequencies than large open oceans (Becker et al. 2020).

Ocean-generated microseism is dominated by surface waves, including Love and Rayleigh waves, which propagate along the Earth's surface. Body waves, such as primary and secondary waves, have a minor role in the generation of ocean-generated microseism (Juretzek & Hadziioannou 2016).

The different generation mechanisms of primary and secondary microseism affect the expected ratio of Love to Rayleigh waves and consequently the amplitude ratio of horizontal to vertical components. Primary microseism exhibits significant and sometimes dominant contributions from horizontally polarised Love waves (Nishida et al. 2008), with the result that the horizontal component is often stronger than the vertical component. Conversely, the generation mechanism of secondary microseism favours the production of Rayleigh waves, resulting in a stronger vertical component (Longuet-Higgins 1950).

2.3 Distributed Acoustic Sensing (DAS)

Distributed acoustic sensing (DAS) allows seismic signals to be recorded along tens of kilometres of optical fibre and over a wide frequency range from below millihertz up to 50 kilohertz (Li et al. 2022). The basic principle of DAS (Figure 2.5 and 2.6) can be broken down into simple steps. Initially, a laser pulse is directed into an optical fibre. As the pulse travels, part of it is backscattered throughout the fibre by Rayleigh backscattering. The backscattered signal is split into two. One signal is delayed by a delay line of a certain length, known as the gauge length, which is 10 m in our particular setup, whereas the other signal is not delayed. The delayed- and the undelayed signals are signals that have been backscattered at two different distances. When the two signals are combined, their interference causes the phase shift between these two signals to be modulated into an amplitude. This amplitude is then sampled. As a result, the time difference between the emission of the laser pulse and the moment of sampling is directly proportional to the distance along the fibre, while the amplitude provides information about the strain over the specified gauge length at the given distance. For a more detailed description of DAS refer to (Li et al. 2022) or (Hartog 2017).
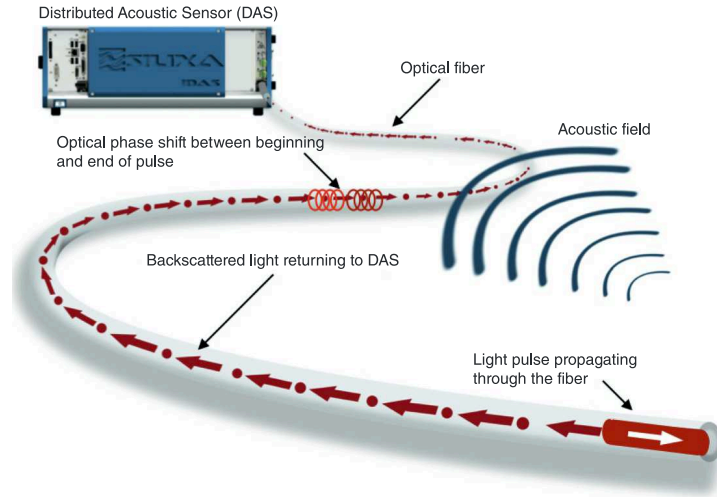

Figure 2.5: The figure shows a DAS device, an optical fibre, a light pulse, the acoustic field straining the fibre, the backscattered light, and the optical phase shift of the backscattered pulse. (Li et al. 2022)
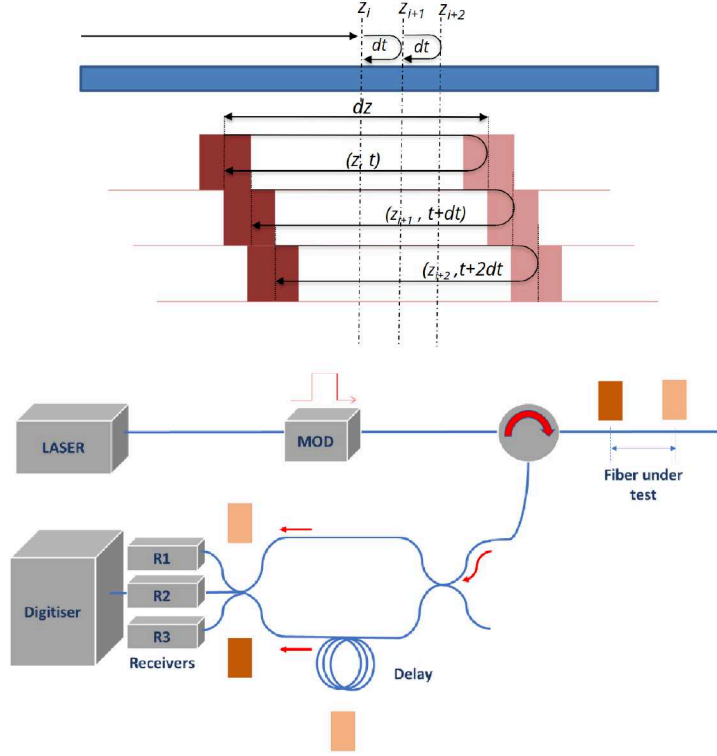
Figure 2.6: Illustration of the measurement principles as well as the gauge length along a fibre and the principal structure of the interrogator. (Naldrett et al. 2018)

DAS has several unique characteristics that differ from those of seismometers. Seismometers typically measure ground motion in terms of velocity, acceleration, or displacement along three orthogonal axes. This triaxial measurement provides detailed information about the direction and intensity of seismic waves at a specific point. In contrast, DAS uses fibre optic cables as sensors and measures strain only along the fibre. This allows DAS to turn the entire fibre into an array of virtual sensors, enabling the continuous monitoring of large areas with high spatial resolution. While seismometers excel in precisely capturing ground motion at specific points, DAS offers the unique ability to detect small changes in strain over long distances.

2.4 European XFEL

A breakthrough in the field of particle accelerators are X-ray free-electron lasers (XFELs), which provide ultra-bright, coherent, and ultra-short X-ray pulses. The free-electron laser facility European XFEL went into operation in 2017. It uses superconducting cavities that allow for the acceleration of many electron bunches at megahertz rate within a pulse (Decking et al. 2020). The European XFEL represents a collaborative effort among multiple European countries to establish a state-of-the-art facility for cutting-edge X-ray research.

The European XFEL consists of four sections (Figure 2.7): The injector, the main linear accelerator (LINAC), the undulator(s), and the experimental beamlines. The injector emits electron bunches and accelerates the beam to 130 MeV. At that energy, the electron bunches are already ultra-relativistic, as they travel at 99.9992% of the speed of light in vacuum. The main LINAC has a length of 1.5 km and accelerates electrons to energies of up to 17.5 GeV. As the electron bunches are already ultra-relativistic before they enter the main LINAC, the speed of the particles barely changes. These accelerated electron bunches are then passed through an undulator, where the electrons travel through an alternating magnetic field, which causes the electrons to emit photons (hard X-ray radiation with a typical wavelength of 0.1 nm). The process in the XFEL's undulator is called Self-Amplified Spontaneous Emission (SASE) (Elleaume et al. 2000) (Geloni et al. 2010). Ultimately, these ultra-intense and ultra-short X-ray photon bunches arrive in the experimental hall and are focused on the sample. Large 2D detectors are used to record the diffraction pattern, for the reconstruction of the structure of large molecules. This way, movies of chemical processes can be captured and analysed. Fast evolutionary experiments are typically carried out in pump-probe arrangements, where external short-pulsed lasers are used to initiate the process, which is then probed by the X-ray pulses.
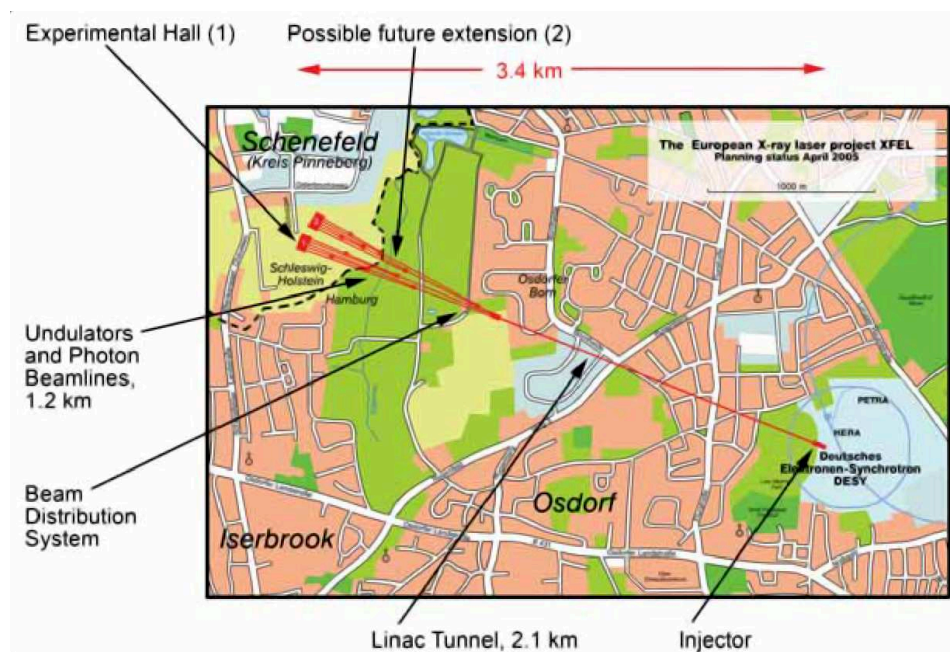
Figure 2.7: Schematic layout of the main components of the European XFEL Facility. (Altarelli et al. 2006)

The European XFEL generates bursts of intense X-ray flashes. These bursts are also called bunch trains, and the European XFEL generates ten bunch trains per second. Within a bunch train, there can be up to 2700 bunches at a rate of 4.5 MHz, resulting in a maximum bunch train duration of 2700/4.5 MHz = 0.6 ms (Czwalinna et al. 2021)

(Figure 2.8). That bunches arrive with low timing jitter is referred to as bunch arrival time stability (Schulz et al. 2019). A good bunch arrival time stability enables higher temporal resolution experiments and is, therefore, an important property for an XFEL. This work aims to enable further improvement of the bunch arrival time stability.
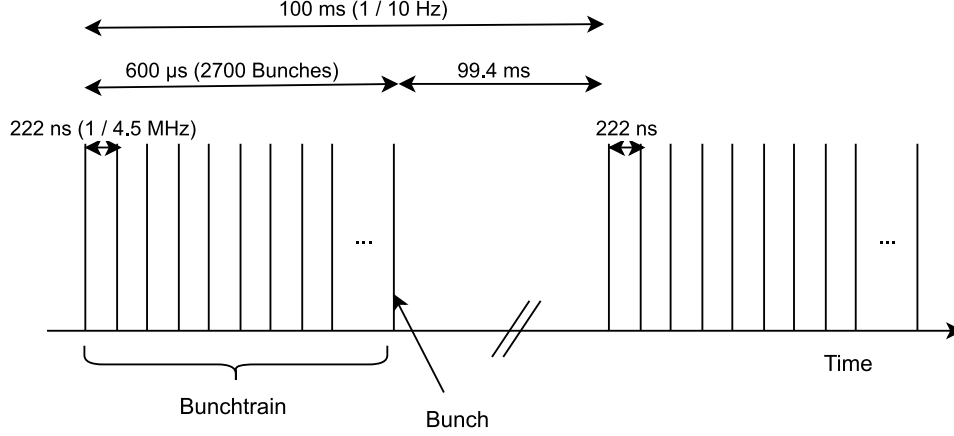

Figure 2.8: Electron bunch time pattern with 10 Hz repetition rate and up to 2700 bunches in a 0.6 ms long bunch train. The electron bunches within a train have a repetition rate of 4.5 MHz. The length of an electron bunch is roughly 200 fs and the non-linear FEL process reduces the duration of a photon pulse to about 100 fs. (Czwalinna et al. 2021)

2.5 Bunch Arrival Time Monitor (BAM)

Along the European XFEL, several monitors called bunch arrival time monitors (BAMs) allow the non-destructive measurement of the arrival time of each individual electron bunch with a resolution of a few femtoseconds. The signals from the BAMs are used for slow and fast feedback loops that stabilise the arrival time of the electron bunches at the end of the accelerator (Schulz et al. 2019). This level of control is essential for the success of a wide range of experiments where even the smallest timing deviations affect the results, making BAMs an indispensable component of accelerator operation.
Here is a brief explanation of how BAMs work (Figure 2.9):

1. An RF antenna picks up the electric field of a traversing bunch and generates a voltage transient with a steep slope in the order of 100 mV/ps.

2. An electro-optical intensity modulator (EOM), based on a Mach-Zehnder type interferometer modulates the voltage transient to optical amplitude with the help of a precisely stabilised optical reference.

3. Analog-digital sampling: Sampling of the optical signal from the EOM and subsequent calculation of the peak amplitudes.

4. Calculation of the timing of each bunch relative to the optical reference using the peak amplitudes.

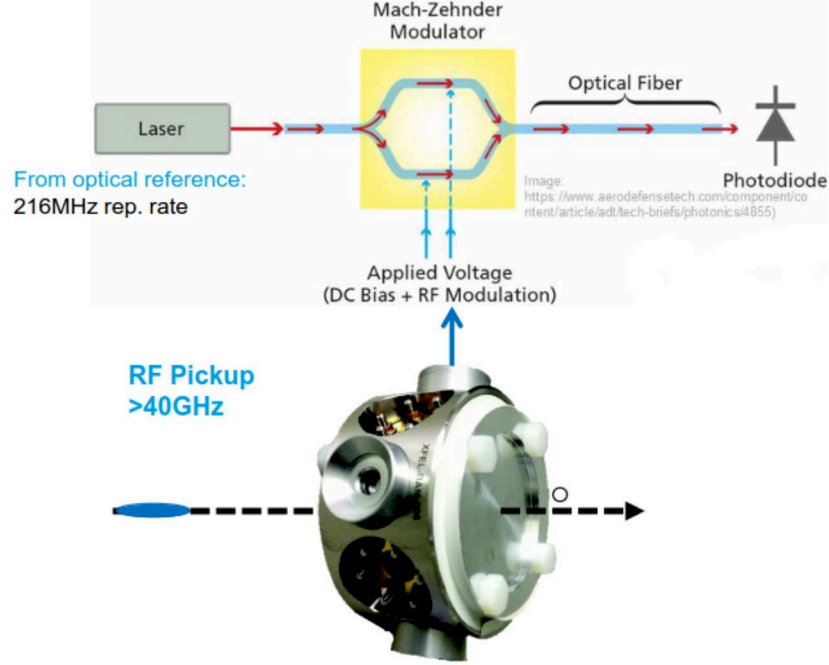In the following each step is described in detail.

Figure 2.9: Working principle of a BAM. At the bottom is a photograph of the RF pickup unit. The beam passes through the RF pickup, which then generates a voltage transient. An electro-optical modulator modulates the transient into an optical amplitude. This is then converted into a voltage by a photodiode. (Angelovski et al. 2015)

1. The RF front end has four pickup antennas, symmetrically mounted onto a metal ring (Figure 2.9). The antennas are located inside the vacuum beam pipe. Their electrical signal is fed into the RF cables via vacuum feed-throughs. The signals from two opposing pickups are combined by using precisely lengthened cables and power combiners. By combining the signals from two opposing pickups, the orbit dependency of the arrival time measurement is significantly reduced (Löhl 2009). The signals from the vertical plane are used as a fine channel since the orbit fluctuations of the electron beam are less pronounced in this direction. The combined pickup signal from the horizontal plane is used as a coarse channel. (Bock 2013) (Angelovski et al. 2012)

2. To modulate the voltage transient to optical amplitude, an electro-optic modulator (EOM) is used.

Laser pulses with a repetition rate of 216 MHz from a femtosecond stable optical reference system are fed into the EOM. The RF signal of an electron bunch passing the pick-up amplitude modulates a single laser pulse of the optical reference. To keep the zero crossing time of the pickup signal in the dynamic time range, an optical delay

line between the optical reference system and the EOM delays the reference pulse with respect to the pickup signal. This delay line also allows the BAM to be calibrated (Dinter 2018) (Dinter et al. 2015).

The EOM requires a laser pulse from the optical reference system. The goal is to modulate an optical pulse whose amplitude represents the time offset between the zero crossing of the RF signal and the laser pulse from the optical reference system (Figure 2.10). Furthermore, an optical delay line between the laser-based optical reference system and the EOM delays the reference pulse with respect to the pickup signal to keep the zero crossing time of the pickup signal in the dynamic time range. This delay line also allows the BAM to be calibrated (Dinter 2018) (Dinter et al. 2015).
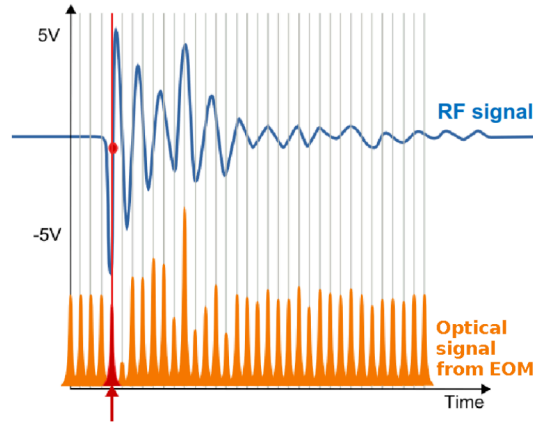

Figure 2.10: The RF signal that is generated by the RF pickup unit of a single bunch and below the optical signal after the electro-optical modulator. (Dinter et al. 2015)

3. To sample the modulated laser pulses from the EOMs, photodiodes are used to convert optical pulses into an electric signal. Two ADCs with a sampling rate of 216 MSPS and 16 bits each are used to measure the peak and the baseline of the photodiode signal. After digitisation, spline interpolation and peak detection are done to obtain the amplitude of the pulse. (Dinter et al. 2015)

4. As Figure 2.10 demonstrates, most of the pulses do not represent bunch arrival times. The bunches arrive at 4.5 MHz, while the pulses have a repetition rate given by the optical reference, which is 216 MHz. So every 48th pulse contains the relevant information (Bock 2013). To determine the actual rate of laser amplitude modulation, not only the pulse that samples the pickup signal, but also the preceding laser pulse has to be taken into account. By subtracting the amplitude that results from no bunch, from the amplitude that results from a bunch arrival, one can remove the offset and obtain the real amplitude modulation (Bock 2013). Furthermore, it is necessary to normalise the real amplitude modulation, using the real amplitude modulation of the previous bunch, with $A_{norm,i} = A_i/A_{i-1}$. This represents a high-pass filter that removes slow amplitude drifts and amplitude jitter from the optical reference. Finally, the resulting amplitude is

multiplied by a calibration constant in order to convert it to a timing change measured in femtoseconds (Bock 2013).

BAMs do not measure absolute bunch arrival time. There is a distance of $1518\,\text{m}$ between BAM.3 and BAM.4.1. Because the bunch train travels at almost the speed of light, it needs $1518\,\text{m}/299\,792\,458\,\text{m/s} \approx 5.06\,\text{µs}$ to travel from BAM.3 to BAM.4.1, while the dynamic range of a BAM is about $1\,\text{ps}$ (Bock 2013). A bunch arrival time monitor detects the arrival of the electron bunch with respect to the optical reference. The laser pulses from the optical reference are distributed throughout the entire accelerator facility in propagation time corrected optical fibres (Schulz et al. 2019). This ensures, that laser pulses from the optical reference system at all BAMs are synchronized with femtosecond precision.

It is important to distinguish between BAM and photon arrival time monitor (PAM). A BAM can only measure the arrival time of electron bunches, whereas a PAM can measure the arrival time of generated photons at the end of the XFEL. PAMs are still under development and are not yet suitable for real-time feedback loops (Kirkwood et al. 2019).

2.6 dCache

dCache is a high-performance, distributed storage system designed to efficiently manage and store large amounts of data. One notable implementation of dCache is found at the Deutsches Elektronen-Synchrotron (DESY), a leading research centre in Germany. At DESY, dCache plays a crucial role in handling the immense volumes of data generated by experiments and research activities, particularly in the field of particle physics. The dCache system at DESY is tailored to meet the specific demands of high-energy physics experiments, ensuring reliable storage, efficient data retrieval, and seamless data management. It optimises data access and retrieval through a distributed architecture, enhancing the overall performance of data-intensive experiments conducted at DESY. (Fuhrmann & Gülzow 2006)

3 Methods

This chapter outlines the procedures and techniques employed in the analysis of seismic and ocean-generated microseism data. It covers all DAS-related methods first, namely the measurement setup, georeferencing, downsampling, and signal processing of iDAS data. This is followed by BAM-related methods: Bunch selection for BAM data and signal processing of BAM data. Next, a description of the seismometer setup is given, and finally the acquisition of numerical ocean wave data from the Wavewatch III model is described.

3.1 iDAS Setup

The so-called intelligent Distributed Acoustic Sensor (iDAS^{TM}) is a device, developed by Silixa Ltd, used by the WAVE initiative, and provided by the group of Prof. Oliver Gerberding of the University of Hamburg. The WAVE initiative investigates and designs a seismic and geo-acoustic measurement network in and around the Science City Hamburg Bahrenfeld. WAVE is an infrastructure for geophysics, physics, and especially for large-scale research facilities (Hadziioannou & Gerberding 2023). iDAS uses the phase of Rayleigh backscattered light to measure dynamic strain events along an optical fibre. iDAS can measure changes in local axial strain down to 10 pm/m resolution and has a signal frequency bandwidth from 1 mHz to 50 kHz (Parker et al. 2014). For information on the general working principle of DAS see Chapter 2.3.

A total of 12 608 m of optical fibres, located on the DESY campus and in the European XFEL, were connected to the iDAS interrogator. The device was installed in Building 35. The fibre runs from Building 35, where the iDAS instrument was located, to the European XFEL. From the injector building (XSIN), through the main linear accelerator tunnel (XTL), through XTD2, XTD9 into the experimental hall. There the fibre is spliced to another fibre of the same cable so that the pulses travel back the same way to Building 35. There, another cable is connected, which runs through cable ducts across large parts of the DESY campus, then alongside the PETRA III tunnel and into Building 35 (Figure 3.1). Here again, two fibres of the cable are spliced together so that the pulses travel back the same way across the DESY campus. The mapping of relevant locations to iDAS channel numbers is described in Chapter 3.2.
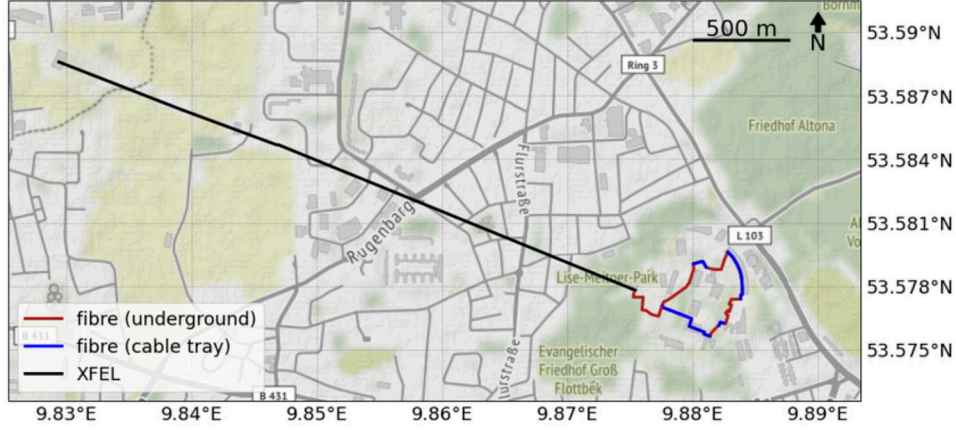
Figure 3.1: Map illustrating the path of the fibre connected to the iDAS instrument. The fibre passes through the PETRA III experimental hall, connecting tunnels, communication shafts, and open cable trays, establishing a fibre loop on the DESY campus. Notably, the fibre passes forth and back through the European XFEL tunnel. (Courtesy: Sandy Croatto)

Within the fibre loop connected to the iDAS interrogator, different optical single mode fibres (SMF) are used. In the European XFEL tunnel from the injector building XSE through the linear accelerator to the SASE beamline tunnel XSE (see Chapter 2.4) a *FTTx A-DQ(ZN)2Y* cable with a *G.657.A* fibre is used. Elsewhere, a cable with the identifier *U-DQ(ZN)BH* and a fibre type *652.D* is used. Both cables are "loose tube", meaning that the fibre is intended to slide inside the cable, which can affect high spatial resolution DAS measurements. These fibres are low bend loss SMF fibres with a damping of $\leq 0.21\,\mathrm{dB/km}$ at $1550\,\mathrm{nm}$.

Configuration parameters of iDAS system:

- Sample rate: $1000\,\mathrm{Hz}$

- Gauge length: $10\,\mathrm{m}$

- Number of channels: $12\,608$

- Bit depth of written data: $16\,\mathrm{bit}$ Integer

- Data rate: $25.2\,\mathrm{MB/s} = 2179\,\mathrm{GB/day}$

3.2 Georeferencing of iDAS data

Georeferencing, in the context of DAS, is the process of assigning geographic locations, such as geo-coordinates, to recorded acoustic events. Georeferencing is an important and sometimes non-trivial task.

To determine the locations of the two relevant BAMs, BAM.3 and BAM.4.1, a colleague went into the tunnel and tapped the tunnel floor next to each BAM with a rubber hammer while the iDAS instrument was running. After calculating the approximate location, these hammer taps can be identified in the data and have been visualised in Figure 3.2. For consistency, the data has been integrated from strain rate to strain. To make the hammer taps visible, the data was high-pass filtered before integration at 100 Hz using the Discrete Fourier Transform (DFT). The RMS strain is expected to be strongest at the channel closest to the hammer impact, which is next to the respective BAM. Therefore, the channel with the highest RMS strain corresponds to the BAM. In the case of BAM.3 it is channel 1445 and in the case of BAM.4.1 it is channel 2955.
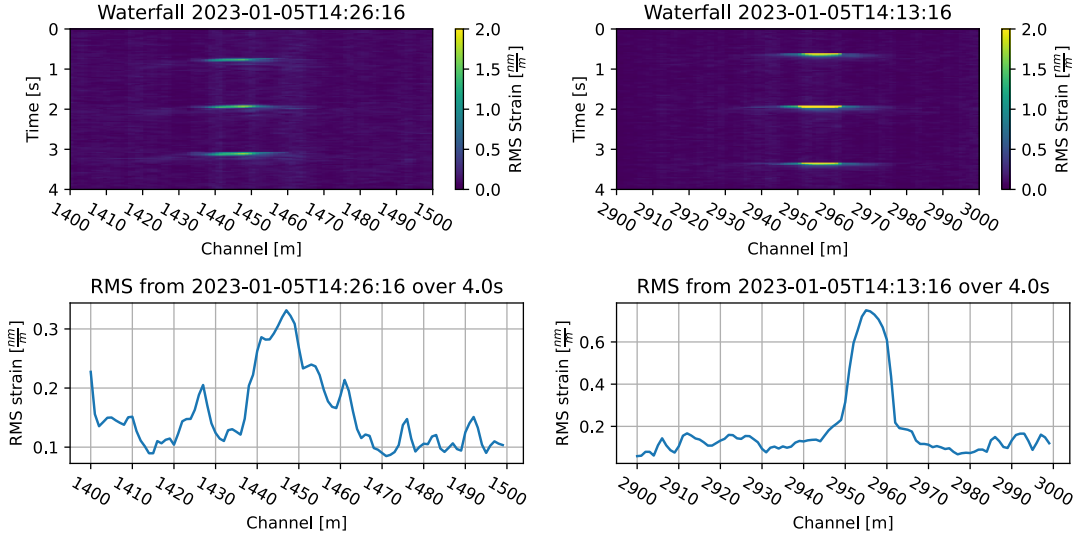

Figure 3.2: Visualisation of hammer taps on the fibre next to BAM.3 (left) and BAM.4.1 (right). The signal is high-pass filtered at 100 Hz. The upper plots show the RMS strain of 20 ms and the lower plots show the RMS strain of the entire selected time. The hammer taps have their strongest effect on channels 1445 and 2955.

3.3 Downsampling of iDAS data

iDAS data was captured from 9 December 2022 to 9 March 2023 (89 days) and from 25 May 2023 to 12 October 2023 (140 days). This is a total of 229 days. During this period, more than 12 km of fibre was connected to the interrogator, resulting in 12608 channels, and the sample rate was set to 1000 Hz. The resulting total amount of data is approximately 460 TB.

A reduced version of the full iDAS dataset is required to allow for a variety of long-term analyses. Otherwise, long-term analyses on iDAS data are impractical due to the large amount of data involved and the resulting excessive computation times. To analyse the effects of ocean waves, a sampling rate of 10 Hz is sufficient. Although the

spatial sampling is one metre, the gauge length is ten metres, so the spatial resolution is somewhere between one and ten metres. Therefore, it is reasonable to downsample the spatial sampling to ten metres in order not to increase the amount of data unnecessarily. For simplicity, the spatial sampling is reduced to $10\,\mathrm{m}$. With a sampling rate of $10\,\mathrm{Hz}$ and a spatial sampling of $10\,\mathrm{m}$, the size is reduced by a factor of 1000, resulting in a size of $460\,\mathrm{GB}$ for the complete dataset. Assuming a read rate of $200\,\mathrm{MB/s}$, the reduced dataset could be loaded into memory within $\frac{460 \times 10^9\,\mathrm{B}}{200 \times 10^6\,\mathrm{B/s}} \approx 38\,\mathrm{min}$. The generation of the reduced dataset is a significant challenge, as the sheer sequential reading of the data would require $\frac{460 \times 10^{12}\,\mathrm{B}}{200 \times 10^6\,\mathrm{B/s}} \approx 27\,\mathrm{d}$.

Naive parallel reading does not provide a significant speed-up, because the bottleneck lies in the storage hardware, not in the network or processing. Since $460\,\mathrm{TB}$ cannot be stored on a single storage device, the key is to exploit the fact that the data is distributed across multiple storage devices. This was accomplished by defining a single read task for each day of data (about $2\,\mathrm{TB}$ per day) and executing these tasks in parallel. As a result, the downsampling of the entire dataset was completed in less than two days using only a single compute node.

Choosing an appropriate downsampling method is an important task before downsampling this large amount of data. An ideal downsampling method reduces the sample rate without distorting the signal components below the new Nyquist frequency, therefore keeping the same frequency and phase spectrum below the Nyquist frequency. To achieve this, high frequency components must be removed in the process otherwise they will cause aliasing artefacts. If the downsampling method is too computationally expensive, the process may not be feasible. In addition, it is important that there are no software errors, because this would waste a lot of valuable computation time. Four different downsampling strategies have been considered and are listed in Table 3.1 with their advantages and disadvantages. Downsampling without anti-alias filtering is not suitable because the aliasing effects are too strong. IIR anti-alias filtering has variable group delay in the passband, which can make interpretation of the downsampled signal very difficult. FIR anti-alias filtering is better in this respect because it has a constant group delay. However, it is computationally expensive and not trivial to implement and must be carefully verified. Another method is called average downsampling. The idea is to take n samples of raw data and calculate the average to retrieve one downsampled sample. For the next sample, the next n samples are used. This reduces the number of samples by a factor of n. In this case, n is 100. Average downsampling is very easy to implement, computationally very cheap, and has a frequency independent group delay. The passband is flat until close to the cutoff frequency, where it has a relatively round roll-off. The downside is the strong side lobes, shown in Figure 3.3, which can lead to aliasing effects if there are very strong signals relatively close to the passband. To check the quality of this downsampling method, Figure 3.4 shows the amplitude spectral density of an iDAS signal before and after applying the downsampling method. There is a slight attenuation near the Nyquist frequency of $5\,\mathrm{Hz}$, but at lower frequencies below $1\,\mathrm{Hz}$ the frequency spectra align almost perfectly. Ocean-generated microseism lies in the $0.05\,\mathrm{Hz}$ to $0.5\,\mathrm{Hz}$ frequency band, where the spectra show remarkable consistency, confirming the suitability of the downsampling approach for the analysis of ocean-generated

microseism.

The same method is used to reduce the number of channels by a factor of ten. The resulting measure represents the average strain rate of 100 m of fibre over 100 ms.

The reduced dataset is now stored in the dCache (Chapter 2.6) and is available to all DESY and WAVE affiliates for extended analyses.
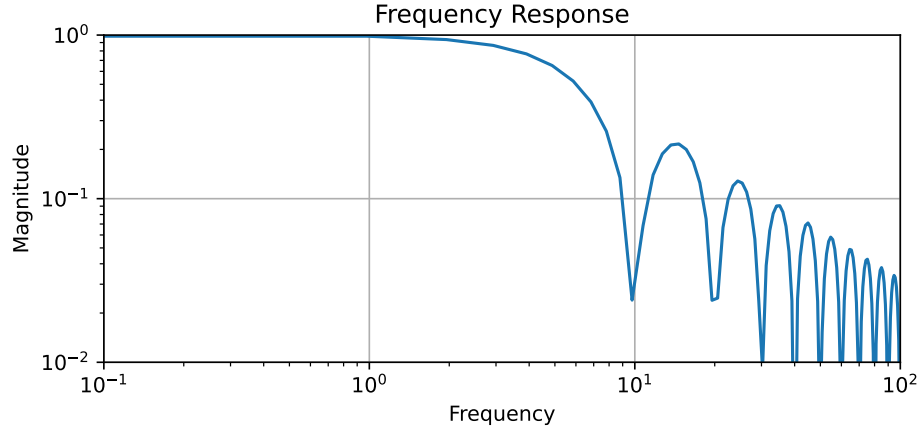

Figure 3.3: Frequency response of a rectangular FIR filter with a window size of 100 samples and a sampling frequency of 1000 Hz. A rectangular FIR filter is the analogue of the average downsampling method but without the actual downsampling. This figure clearly shows the disadvantages of this filtering method, namely low attenuation in the stopband (strong side lobes) and a round roll-off.
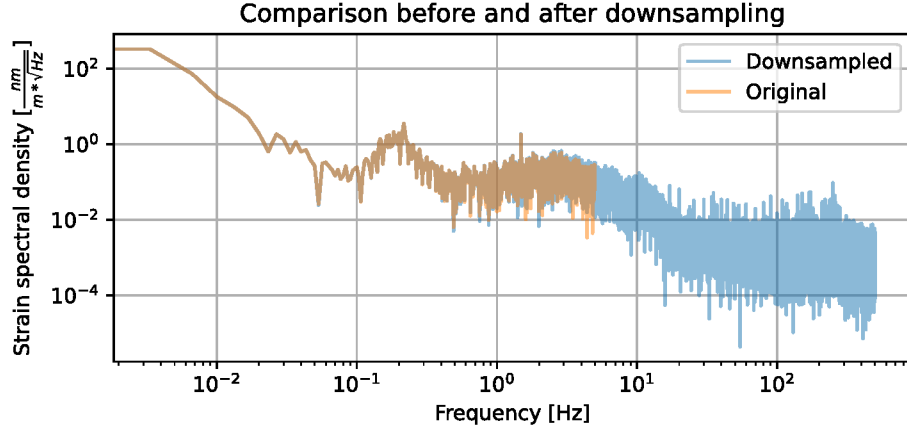
Figure 3.4: Frequency spectra comparison of iDAS data before and after downsampling. The objective is to assess whether the average downsampling method introduces any aliasing effects or distortions in the frequency spectrum. The average of ten channels within the LINAC of the European XFEL was calculated to reduce instrument noise. Then the data is downsampled using the average downsampling method. The spectra were calculated from 5 minutes of data with 1000 Hz before downsampling and 10 Hz after downsampling.

Method	Advantage	Disadvantage
Downsampling without anti-aliasing	+ Easy to implement, not prone to errors. + Computationally fastest method conceivable.	- Strong aliasing effects when high frequency content is present.
Average downsampling	+ Constant group delay. + Computationally efficient. + Easy to implement, not prone to errors.	- Aliasing effects are not as strongly filtered as with the following methods.
IIR anti-aliasing filter (Butterworth or Bessel) followed by downsampling	+ Very good attenuation of aliasing effects. + Moderate computational efficiency.	- Variable group delay in the passband.
FIR anti-aliasing filter followed by downsampling	+ Constant group delay. + Good attenuation of aliasing effects	- Filter design is a complex task that may require verification. - Computationally expensive.

Table 3.1: Different downsampling strategies, considered. Ordered by computationally fast (top) to slow (bottom), and signal quality good (top) to bad (bottom).

3.4 Signal processing of iDAS data

For the analysis in this work the downsampled dataset, described in Chapter 3.3, is used. This dataset is already downsampled to 10 Hz, therefore matching the sample rate of the BAM data and avoiding excessive computation times. To calculate the average strain of the European XFEL between BAM.3 and BAM.4.1, the corresponding channels have been averaged. The process of finding the channel corresponding to a given location is referred to as georeferencing and is described in Chapter 3.2. By first calculating the mean of the selected channels, the amount of data is further reduced and computation time is saved. The result is a one-dimensional time series.

iDAS measurements are sensitive to variations in the temperature of both the instrument and the fibre. BAM measurements, on the other hand, are not sensitive to temperature induced changes and therefore it is necessary to remove the temperature drifts from the iDAS signal, in order to compare the two measurements. To remove temperature drifts, a high-pass filter has been applied. Raw iDAS data is stored as analog-digital-converter (ADC) counts which are proportional to the strain rate of the fibre. To obtain actual strain rate, the raw data must be multiplied by a calibration constant. The resulting unit is $\frac{nm}{m \cdot s}$. In the downsampled dataset this is already done (Chapter 3.3). The bunch arrival time difference between two BAMs is proportional to

the strain of the tunnel section if the given signal is of seismic origin. To convert the iDAS data from strain rate into strain, it is integrated in time. This also scales the signal by 1/frequency which reduces high frequency noise but greatly amplifies temperature drifts. The spectra of both systems are visualised in Figure 4.7.

Effectively removing temperature drifts from iDAS measurements is a tricky task, as temperature drifts are typically many orders of magnitude stronger than ocean-generated microseism in strain data. While ocean-generated microseism is generally not below 0.05 Hz, temperature-induced changes have orders of magnitude lower frequencies. In some cases, there is no periodic character at all. Because of the frequency difference, temperature drifts can be removed by high-pass filtering. Four different filter methods have been considered to remove temperature drifts. Linear detrending is a linear regression of the selected data period and removal of the calculated slope. Linear detrending works well for short periods in most cases, but its effectiveness depends on the duration of the data. FIR filters do not have this problem, but due to the low frequency and high attenuation required, the resulting filter kernel is impractically long compared to the signals being analysed. IIR filters generally have a frequency dependent group delay, which would make them unsuitable. It is possible to mitigate this and achieve zero group delay by applying the IIR filter to the reversed signal as well. However, the attenuation of temperature drifts is not as strong and the cutoff is not as sharp, as with other methods. Finally, the Discrete Fourier Transform (DFT) is used to transform the signal into frequency domain for filtering and back again. This method produces a very sharp frequency cutoff. Strong spectral smearing effects can occur due to the large magnitude of temperature drifts, which is avoided by applying this method before integration from strain rate to strain. The selected cutoff frequency is 0.05 Hz. This method effectively removes the temperature effects while introducing the least amount of filter artefacts.

3.5 Bunch selection for BAM data

The European XFEL produces X-ray trains at a rate of 10 Hz. Within one train, there can be up to 2700 ultra-short X-ray flashes. A FEL creates electron bunches first which are used in later tunnel sections, called undulators or SASEs, to produce X-ray flashes. There one electron bunch results in one X-ray flash. A BAM measures the relative arrival time of each individual electron bunch within a bunch train. The bunch train is divided into different beam regions, which can have different properties. A beam region can be stabilised by a feedback system. For the experiments of this thesis, it is important that only bunches from a stabilised beam region are used. The feedback system needs some time to achieve sufficient stability and suffers from the transition to the next beam region. Therefore, the first and last 50 bunches of a beam region are not used in the experiments of this thesis.

3.6 Signal processing of BAM data

BAM measurements are stored for two weeks in the data acquisition system (DAQ) of the European XFEL. A digital infrastructure designed for the collection and management of experimental data generated by the operation and experiments conducted at DESY (Agababyan et al. 2007). After extracting the data from the DAQ, the samples (bunch trains) have to be sorted by their unique bunch-train-id. The sample rate is 10 Hz, since the European XFEL accelerates ten bunch trains per second. Some samples are missing due to the high system load of some components in the tunnel. This accounts for up to 2%, depending on the time and the BAM. The missing samples are substituted using cubic spline interpolation. Linear interpolation was also considered, but in this case, the resulting signal quality is generally better with cubic spline interpolation, and the additional computational effort is not significant because of the preceding data reduction. Depending on the configuration of the European XFEL, bunches are not generated at the full 4.5 MHz. In some cases, every second potential bunch is omitted, resulting in zero values in the BAM data. To mitigate this, all bunches that are zero over the entire selected time interval, are removed. Ocean-generated microseism strains the tunnel. The absolute arrival time is influenced by many other factors overlaying the strain of the tunnel. A measure that is proportional to strain is the (relative) bunch arrival delay between two points in the accelerator tunnel. This is retrieved by calculating the difference between the arrival times at two BAMs. Even this difference does not represent the absolute delay, but only a relative, as described in Chapter 2.5. However, the relative delay is good for comparison with iDAS, as iDAS also measures relative instead of absolute strain. Finally, an interval of bunches per bunch train is selected for averaging. Averaging reduces the noise floor below the ocean-generated microseism amplitudes. Only bunches from a stabilised beam region with feedback loops should be used to achieve low noise results. A stabilised beam region can be identified by its low arrival time jitter within a bunch train. In Figure 4.5 the stabilised beam region is visible as a horizontal region and the selected bunch interval is highlighted in green.

3.7 Seismometer Setup

The Güralp Systems CMG-3TD is a three-component digital broadband seismometer. The instrument is a well-proven, established design based on the 3T seismometer and the DM24 digitiser. The frequency response is within 3 dB or better from 0.009 Hz to 50 Hz on all three axes (Figure 3.5). In the ocean-generated microseism frequency band from 0.1 Hz to 0.3 Hz the attenuation is close to 0 dB. Therefore, this seismometer is well suited to measure ocean-generated microseism.
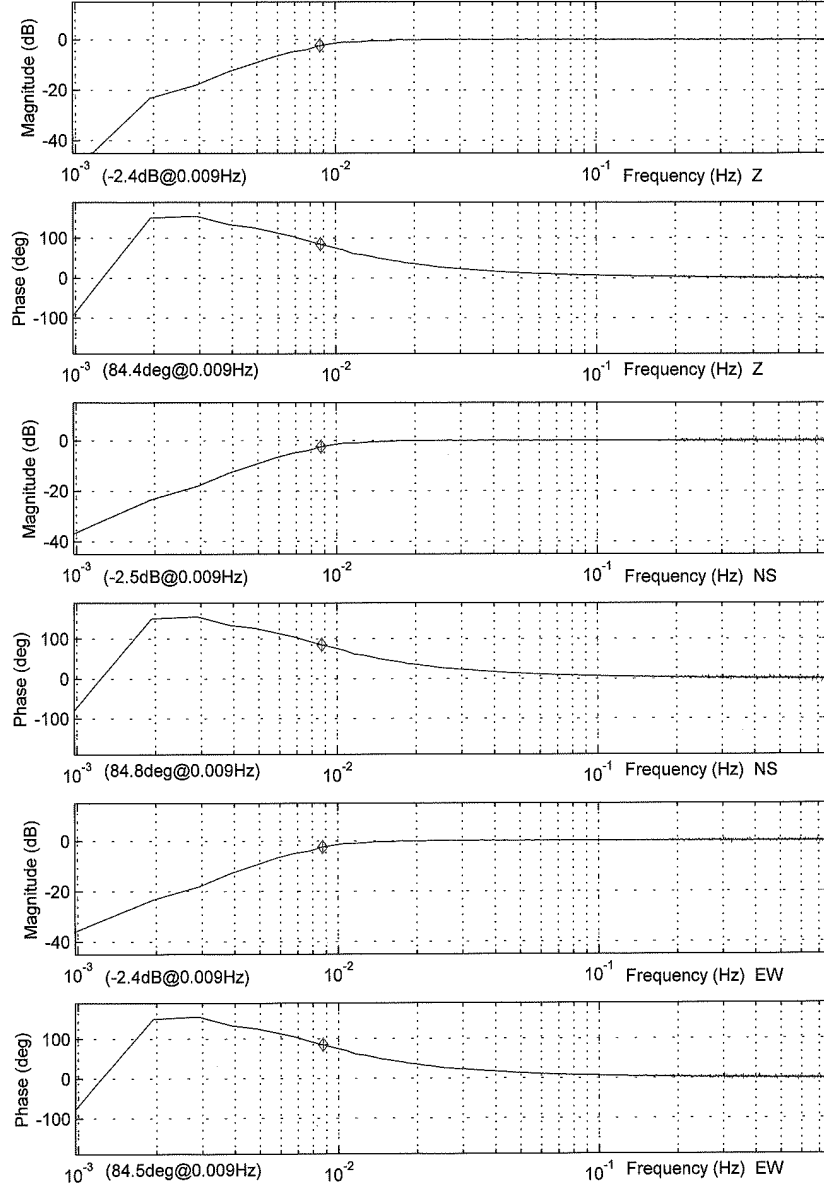
Figure 3.5: Normalised lower-end frequency response from the calibration of this individual seismometer. (Gü 2019)

The placement of a seismometer is generally very important and can strongly influence the measurement. It is located in the injector building of the European XFEL (Chapter 2.4), called XSIN (Figure 3.6). There it is in the 7th underground level at NN+7.6 m, which is 29.4 m below the surface. The seismometer stands on a concrete floor about 2 m thick (Figure 3.7). Below the floor is the secondary injector tunnel, and further below is the primary injector tunnel that is in use today. As a result, some of the injector noise may be coupled into the measurement. However, the heavy concrete plate can absorb much of the higher frequency noise, creating a relatively quiet measurement situation, which helps to measure lower frequency motions such as ocean-generated microseism.
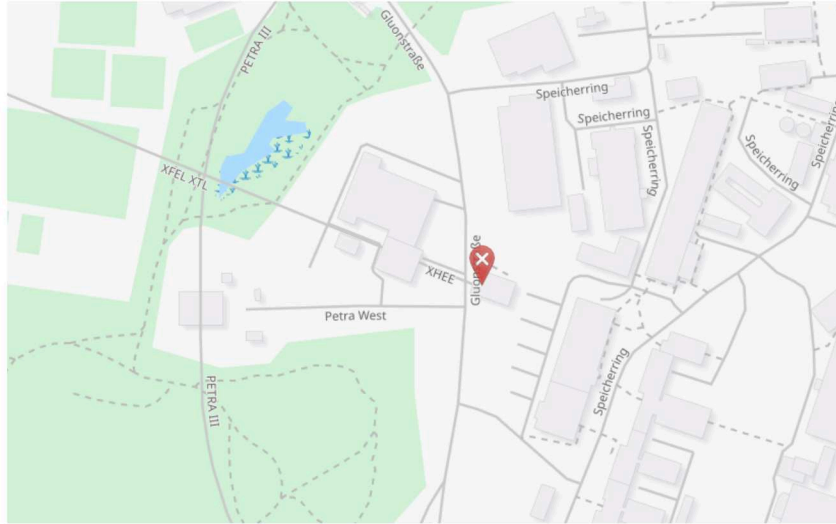
Figure 3.6: Location of the seismometer, which is installed in the European XFEL's XSIN building, on a map.

Figure 3.7: The installation site of the seismometer in the 7th underground level of the XSIN building of the European XFEL. (Courtesy: Norbert Meyners)

3.8 Acquisition of numerical ocean-wave data from Wavewatch III model

Wavewatch III (WW3) is a numerical wave model designed to simulate and forecast ocean waves. The model is designed to provide forecasts of various wave parameters such

27

as wave height, wave direction and wave period on a global scale (Tolman et al. 2009). It is widely used in oceanography, marine forecasting and climate research (Bi et al. 2015). Wavewatch III was developed by researchers at the National Centers for Environmental Prediction (NCEP), part of the National Weather Service (NWS) in the United States. The model has undergone several updates and improvements since its initial release. The primary purpose of Wavewatch III is to simulate ocean surface waves and provide forecasts that are useful for a variety of applications, including maritime operations, coastal engineering, and climate research. It helps to understand the behaviour of waves under different atmospheric and oceanic conditions. Wavewatch III is a numerical model that represents the physical processes involved in wave generation, propagation and dissipation. It takes into account factors such as wind speed, atmospheric pressure, and sea ice conditions (Tolman et al. 2009). The model has global coverage, allowing it to simulate wave conditions in oceans and seas around the world. This makes it valuable for a wide range of applications, including shipping, offshore operations, and coastal management. Wavewatch III provides forecasts of several wave parameters, including significant wave height, wave period and wave direction. These parameters are essential for understanding the characteristics of ocean waves and their potential impact on various activities.

For the purpose of this thesis, the simulation results were retrieved from `earth.nullschool.net`, an easy-to-use tool that visualises various environmental data, including ocean wave data, using models such as Wavewatch III. The data displayed on earth.nullschool.net is not calculated or generated by the website itself. Instead, it pulls data from various sources, including numerical weather prediction models such as Wavewatch III, and presents it in a visual and interactive format (Beccario 2015).

4 Results

This chapter presents the results of the data analyses performed which demonstrate and evaluate the impact of ocean-generated microseism on the performance of the European XFEL. The chapter is divided into four sections. The first gives an overview of the ocean-generated microseism over almost one year, using iDAS data, revealing a strong seasonal dependence. The second section proves that the noise observed at the European XFEL is of seismic origin by comparing BAM and iDAS measurements. The third section incorporates seismometer data, to gain a deeper understanding of the geophysical properties and the generation mechanism of the observed ocean-generated microseism. In the fourth section, the seismometer data is compared with numerical ocean wave data simulated by the Wavewatch III model (Tolman et al. 2009) to validate the previous results and to determine the source of the observed ocean-generated microseism.

4.1 Long-term characteristics

Ocean-generated microseism is supposed to have a strong seasonal dependence. To search for seasonal variation in the iDAS measurements, the whole iDAS dataset, including measurements from December 2022 until September 2023 (inclusive) was visualised. As a first step, the complete 460 TB of iDAS data were downsampled by averaging to a frequency of 10 Hz and a spatial pixel size of 10 m, resulting in a dataset of 460 GB, as explained in Chapter 3.3. Exactly those channels that correspond to the tunnel section from BAM.3 to BAM.4.1, as explained in Chapter 3.2, are selected and averaged to a one-dimensional time series. In order to have units consistent with the other experiments, the strain rate data is integrated to strain. The resulting measure represents the average strain of the relevant tunnel section. From this prepared data the spectral density is calculated using sliding windows with a size of $2^{15} = 32768$ samples (3276.8 seconds). Spectral smearing was reduced by prior multiplication with a Hanning window function.

The spectral density data is visualised in several ways. Figure 4.1 shows the full spectrogram. For the visualisation of the spectrogram, nearest-neighbour interpolation was used. Figure 4.2 and 4.3 show RMS from 0.05 Hz to 0.5 Hz, representing ocean-generated microseism. Figure 4.3 shows the RMS of the ocean-generated microseism spectrum. It contains annotations for all earthquakes worldwide with a magnitude of six or greater. The earthquakes are retrieved from the United States Geological Survey (USGS) earthquake catalogue (Guy et al. 2015).
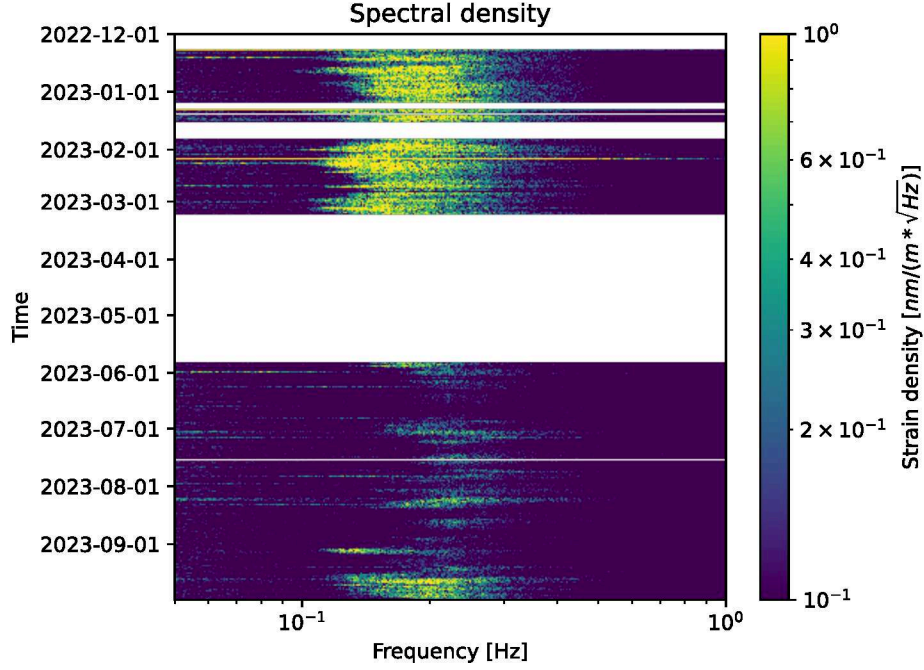
29

Figure 4.1: Spectrogram made from the mean of channels that correspond to the LINAC tunnel section between BAM.3 and BAM.4.1 of the entire iDAS dataset. The frequency band is selected to show ocean-generated microseism. The measurement setup is described in Chapter 3.1. There is a prominent seasonal contrast between summer and winter. The horizontal stripes are caused by earthquakes due to their broad frequency spectrum, high intensity, and short duration. Blank areas indicate periods with no data available. Notably, during March, April, and May the iDAS was utilised for another experiment.
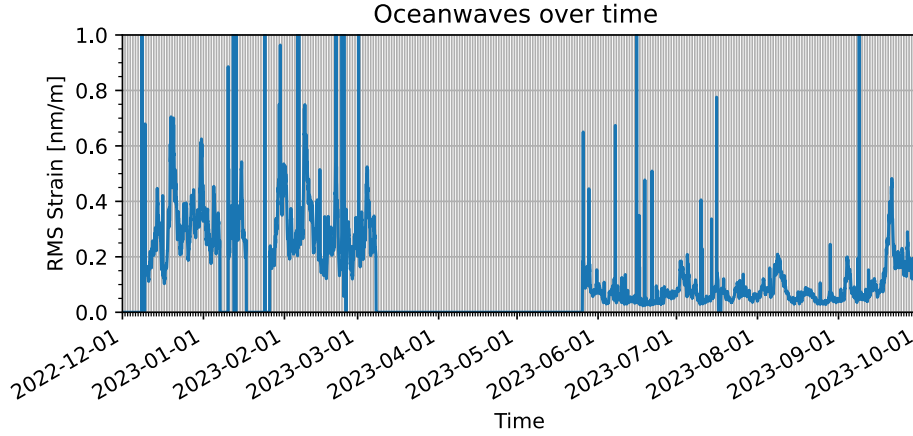
Figure 4.2: RMS of the ocean-generated microseism frequency band (0.05 Hz to 0.5 Hz), showing the entire iDAS dataset. Based on the data shown in Figure 4.1. The spikes are most likely caused by earthquakes.
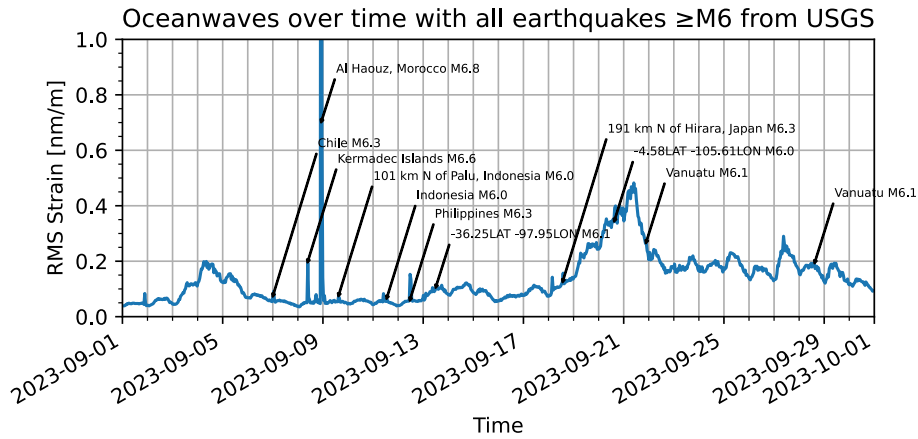

Figure 4.3: Zoomed version of Figure 4.2, showing September only. It contains annotations for all earthquakes worldwide with a magnitude of six or greater. The earthquakes are retrieved from the United States Geological Survey (USGS) earthquake catalogue (Guy et al. 2015). The spikes without annotations are most likely caused by lower-magnitude earthquakes.

During some periods iDAS measurement data is missing. In Figure 4.1 missing data is visualised as white areas. During winter the instrument was set up and different ways of collecting and transferring the data to the permanent storage system dCache (Chapter 2.6) had to be figured out. This is the reason for the data leaks in December. During March, April, and early May, the iDAS was used for another experiment.

Ocean-generated microseism depends on weather conditions. On the North Atlantic and North Sea, winds are significantly stronger in winter, than in summer, as shown in

Figure 4.4. The iDAS measures 0.35 nm/m RMS in December, while it is only 0.06 nm/m RMS in June, which is a factor of six in difference (Figure 4.2). We do not have continuous long-term measurements from the BAM system, because the accelerator is sometimes switched off for maintenance, has to be commissioned, or tuned to find good operation settings. From Chapter 4.2 we know the relation between strain and bunch arrival time. Therefore, the impact corresponds to 3.5 fs RMS in December and 0.6 fs RMS in June. It is important to note that this is the RMS over the whole month. Within a month there is a high variation of the strain and bunch arrival time stability (Figure 4.2). As a consequence, the peak effects are much higher, as shown in Chapter 4.2. Finally, there is significantly stronger ocean-generated microseism during winter and therefore a better bunch arrival time stability can be expected during the summer.
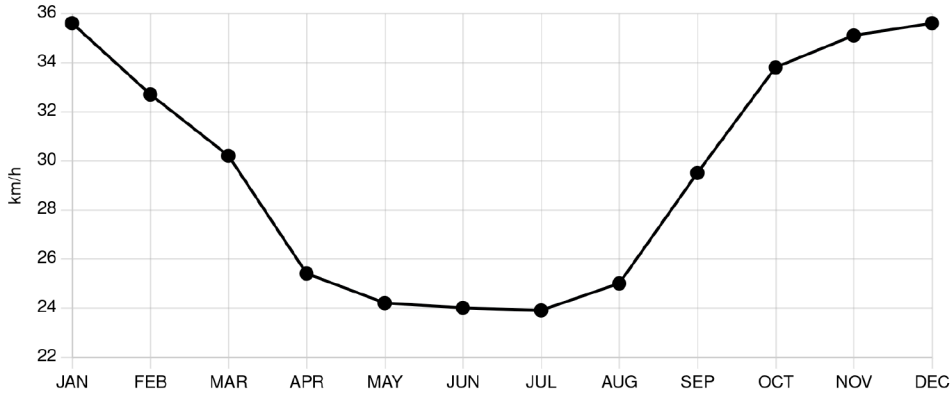

Figure 4.4: Average wind speeds from 1991 to 2020 at Helgoland for each month of the year. A clear summer-winter difference is visible, with about 24 km/h in the summer months (May, June, July) and about 35 km/h in the winter months (October, November, December, January). (Meteostat 2024).

Earthquakes are very energetic and have a very broad frequency spectrum (Rathje et al. 1998) and are therefore visible in the ocean-generated microseism frequency band. Figure 4.3 reveals that the spikes in the ocean-generated microseism spectrum are caused by earthquakes. In Figure 4.1 earthquakes cause horizontal stripes, due to their broad frequency spectrum, high intensity, and short duration. The peak on 9 September was caused by the prominent 6.8 magnitude earthquake in Morocco. This quake caused exceptionally strong strain at the European XFEL, not only because of its magnitude but also because of its proximity. All earthquakes in September with a magnitude of 6 or greater are annotated in Figure 4.3. This covers most of the peaks. The other peaks could be weaker earthquakes. The fact that some strong earthquakes show only a small peak in the given frequency interval could have several reasons, such as the depth of the quake, the distance of the quake, and the frequency spectrum of the quake, which could be outside the selected frequency interval. On closer inspection, unannotated spikes remain that are stronger than some annotated spikes. These could be weaker earthquakes that are closer to the European XFEL and/or better match the selected frequency range.

In September, data was collected from as many instruments as possible to allow for a wider range of analysis. Figure 4.3 shows that there were two periods with strong signals in the ocean wave frequencies. These are the 4th of September, with weaker and very low frequency signals, and the 21st of September, with stronger and higher frequency signals. These two periods are analysed in further detail in this chapter, incorporating measurements from iDAS, BAM, and seismometers. Although not used in this thesis, data from the LBSync system was also collected. For information on the LBSync system see (Bock 2013).

4.2 Comparison of bunch arrival time with physical strain (iDAS)

Strong bunch arrival time jitter can be observed at the European XFEL within the frequency range from $0.05\,\mathrm{Hz}$ to $0.5\,\mathrm{Hz}$ (Figure 4.7). This analysis reveals that the observed jitter in bunch arrival time can be accurately measured using the iDAS instrument, indicating its seismic origin.

By averaging the measured arrival times of several bunches, it is possible to significantly reduce the BAM measurement noise so that even weak ocean-generated microseism can be detected. It is important that only bunches within a stabilised beam region are used. How the bunches are selected is described in Chapter 3.5. Figure 4.5 shows the arrival times of all bunches of several complete bunch trains at the two relevant BAMs. The selected bunches are highlighted in green.
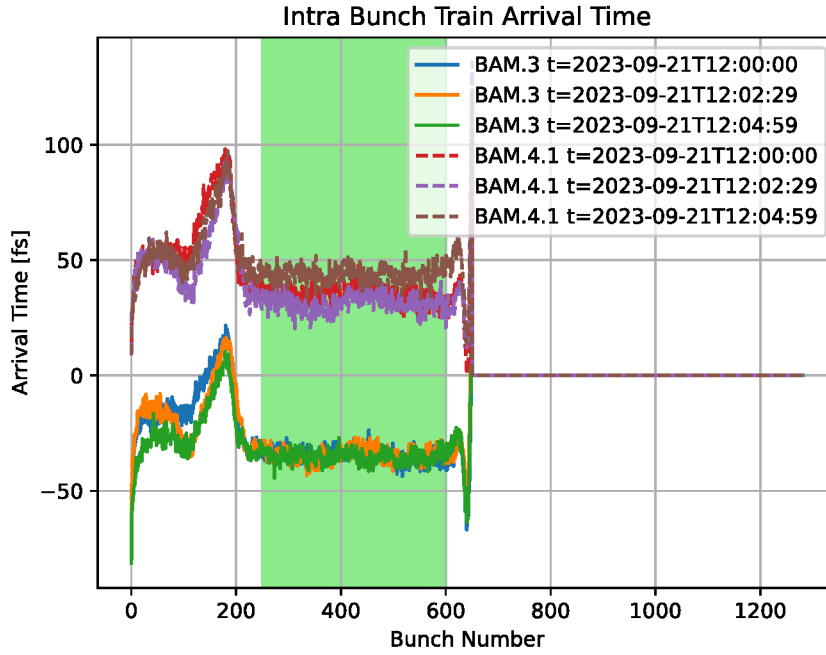
Figure 4.5: Relative bunch arrival time over the bunch number for three different bunch trains, starting at 12:00 CEST. More information on bunches and bunch trains can be found in Chapter 2.4. The bunches are separated into different regions for different purposes. The region with the feedback system switched on has a very stable bunch arrival time and is therefore nearly constant. The selected bunch region for the analyses in this chapter is marked in green.

In order to obtain a measure from BAMs that can be compared with strain measurements from iDAS, the difference between the averaged measurements from two different BAMs is calculated. The measured strain is supposed to be proportional to the bunch arrival time difference.

Figure 4.6 shows the high-pass filtered strain measured by iDAS at the relevant channel numbers. The signal processing performed is described in detail in Chapters 3.3 and 3.4. Ocean-generated microseism is visible in the form of horizontal lines with periods of five to six seconds. These lines are not perfectly horizontal. They have a slight slope of about 2 s per 1000 m. A closer look at the ocean waves reveals a modulation in amplitude with a period of about 30 s. In addition to that, there is a strong signal around channel 2400, caused by car traffic on the road *Rugenbarg*, which is perpendicular to the tunnel. To the right of channel 2400, after 60 seconds, cars are driving on a smaller road called *Bornheide*, which is almost parallel to the tunnel (a map is shown in Figure 2.7). It turns out that car signals always affect some channels positively and others negatively, giving a sum of zero, considering all channels of one time-sample. This allows car traffic signals to be cancelled out by calculating the average of all channels shown.
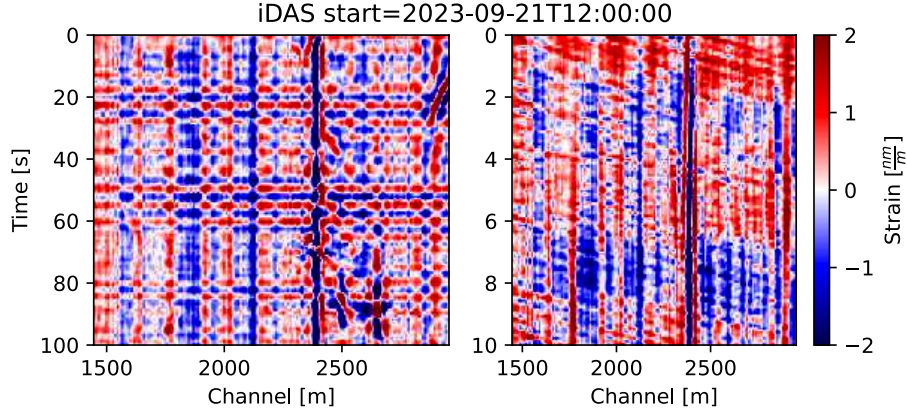
Figure 4.6: Waterfall diagram of iDAS data starting at 12:00 CEST. The displayed channels correspond to the section between BAM.3 and BAM.4.1. After subsampling to 10 Hz by averaging, the data is high-pass filtered at 0.05 Hz to remove strong, slow temperature drifts. The right figure is a zoomed version (in the time axis) of the left figure. Ocean-generated microseism is visible as almost horizontal lines, with periods of five to six seconds.

The seismically induced bunch arrival time difference between two BAMs is expected to be directly proportional to the accelerator strain between these BAMs. The expected proportional factor depends only on the distance between the BAMs d and the velocity of the electrons c, which is very close to the speed of light in vacuum as shown in Chapter 2.4. BAM.3 is located at 414 m and BAM.4.1 at 1932 m along the European XFEL, so the distance is $1932\,\text{m} - 414\,\text{m} = 1518\,\text{m}$. Formula 4.1 shows that a change of $1\,\frac{\text{nm}}{\text{m}}$ in strain is expected to result in a delay of about 5 fs in the bunch arrival time.

$$t = \frac{e \cdot d}{c} \Rightarrow t = \frac{1\,\frac{\text{nm}}{\text{m}} \cdot (1932\,\text{m} - 414\,\text{m})}{299\,792\,458\,\frac{\text{m}}{\text{s}}} \approx 5.064\,\text{fs} \qquad (4.1)$$

Using the correlation factor of Formula 4.1, the frequency spectra of the measured bunch arrival time difference and the iDAS data can be compared. Figure 4.7 shows the frequency spectra of both measurements without high-pass filtering. Strong low frequency signals are caused by the temperature sensitivity of iDAS and are not visible in the BAM spectrum. At higher frequencies, the spectra are in good agreement. The ocean-generated microseism peak is visible at 0.18 Hz and matches the strong secondary ocean-generated microseism peak in the seismometer measurements shown in Figure 4.10c. Unlike the seismometer data in Figure 4.10d, this visualisation shows no significant primary ocean-generated microseism peak. The data remains in their respective units, fs and nm/m, but the scales are shifted so that 1 nm/m corresponds to 5 fs as derived from Formula 4.1. Therefore, the scales are aligned such that the signal amplitudes are supposed to match, but the comparison reveals a discrepancy.
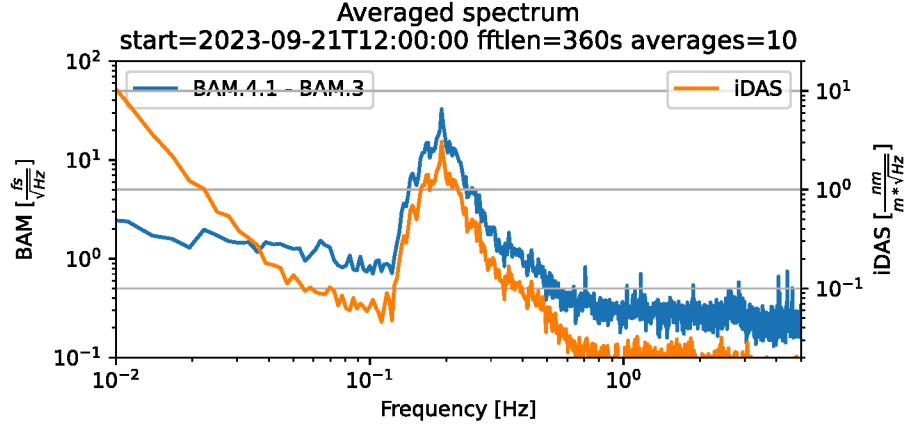
Figure 4.7: Comparison of BAM and iDAS frequency spectra for one hour of data, starting at 12:00 CEST. The iDAS spectrum is based on the average of all channels corresponding to the section between BAM.3 and BAM.4.1 (Chapter 3.2), whereas the BAM data represents the difference of the arrival times at BAM.4.1 and BAM.3, averaged over the selected bunches marked in green in Figure 4.5. For this visualisation, the iDAS data is not high-pass filtered. The data remains in their respective units, fs and nm/m. But the scales are shifted, so that 1 nm/m corresponds to 5 fs as derived from Formula 4.1.

Formula 4.1 derives the expected linear correlation factor. Despite that, the actual correlation factor for this measurement is calculated as shown in Figure 4.8. First, the cross-correlation is calculated to find and compensate for offsets. Second, the correlation factor is calculated using linear regression. Compensating for time offsets first is an important step to ensure the validity of the linear regression. The correlation factor resulting from the linear regression is $9.534 \frac{\text{fs}}{\text{nm/m}}$, which is 88% higher than the expected factor of $5.064 \frac{\text{fs}}{\text{nm/m}}$ (Formula 4.1). The possible sources of this discrepancy are discussed in Chapter 5. After scaling the iDAS data by the factor $9.534 \frac{\text{fs}}{\text{nm/m}}$, the BAM data correlates very well with the iDAS measurements (Figure 4.9). Apart from the discrepancy in the linear correlation factor, the very good correlation proves that the noise in the 0.05 Hz to 0.5 Hz frequency band has a seismic origin.
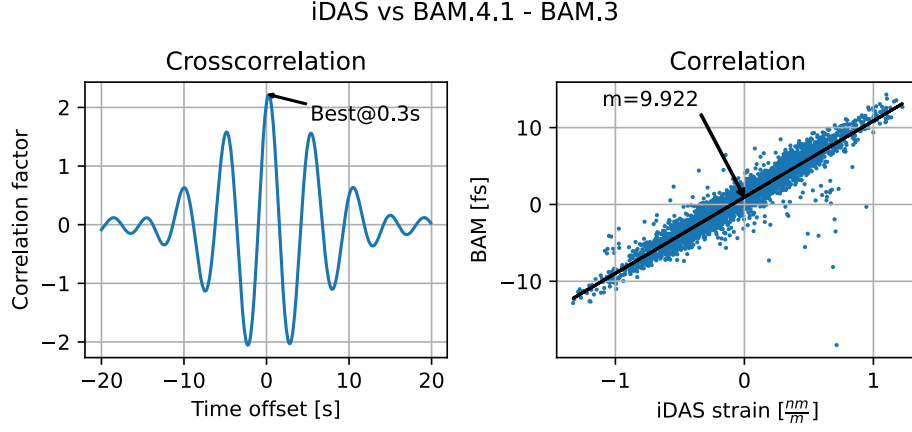
Figure 4.8: Correlation of BAM with iDAS data using a time window of 300 s (3000 samples each), starting at 12:00 CEST. The BAM data represents the difference of the arrival times at BAM.3 and BAM.4.1, averaged over the selected bunches as shown in Figure 4.5, while the iDAS data is mean-downsampled to 10 Hz, averaged over the relevant channels (Chapter 3.2) and high-pass filtered at 0.05 Hz to remove temperature drifts against which BAM measurements are insensitive. First, the cross-correlation (shown above) is calculated to correct for time offsets. Second, the correlation plot (shown below) was created and linear regression was performed. The correlation factor resulting from the regression is $9.534 \frac{\text{fs}}{\text{nm/m}}$, which is 88% more than the expected factor of $5.064 \frac{\text{fs}}{\text{nm/m}}$ (Formula 4.1).
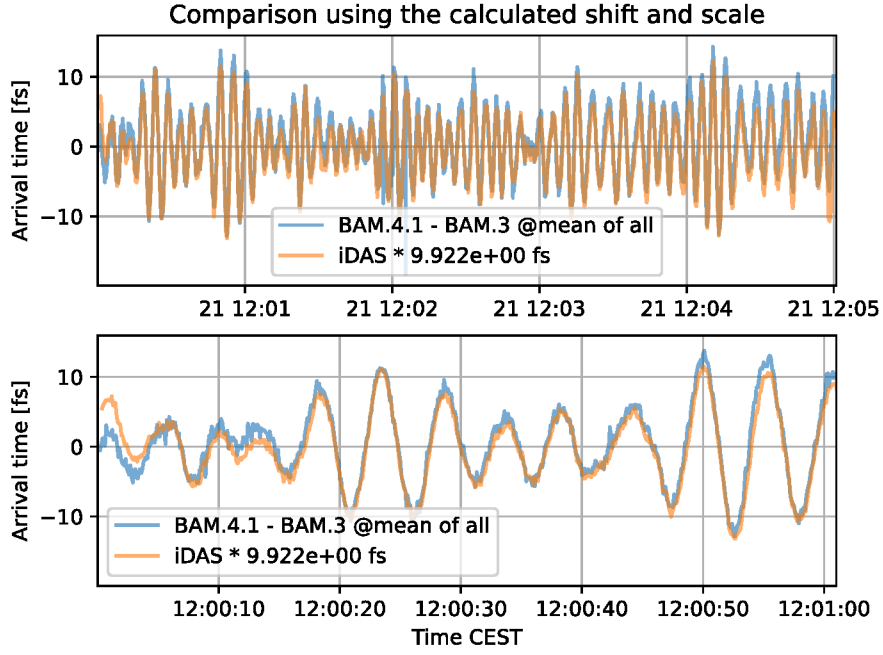
Figure 4.9: Comparison of BAM and iDAS data in the time domain. The top figure is a zoomed version of the bottom one. The BAM data represents the difference of the arrival times at BAM.3 and BAM.4.1, averaged over the selected bunches as shown in Figure 4.5, while the iDAS data is mean-downsampled to 10 Hz, averaged over the relevant channels (Chapter 3.2) and high-pass filtered at 0.05 Hz to remove temperature drifts against which BAM measurements are insensitive. The iDAS data is scaled with the correlation factor calculated by linear regression, as shown in Figure 4.8. The signals are dominated by ocean-generated microseism and show an amplitude of up to 24 fs peak-to-peak. However, there is an amplitude modulation with a period of about 30 s.

4.3 Wave-type based on seismometer data

(a)

(b)

(c)

(d)
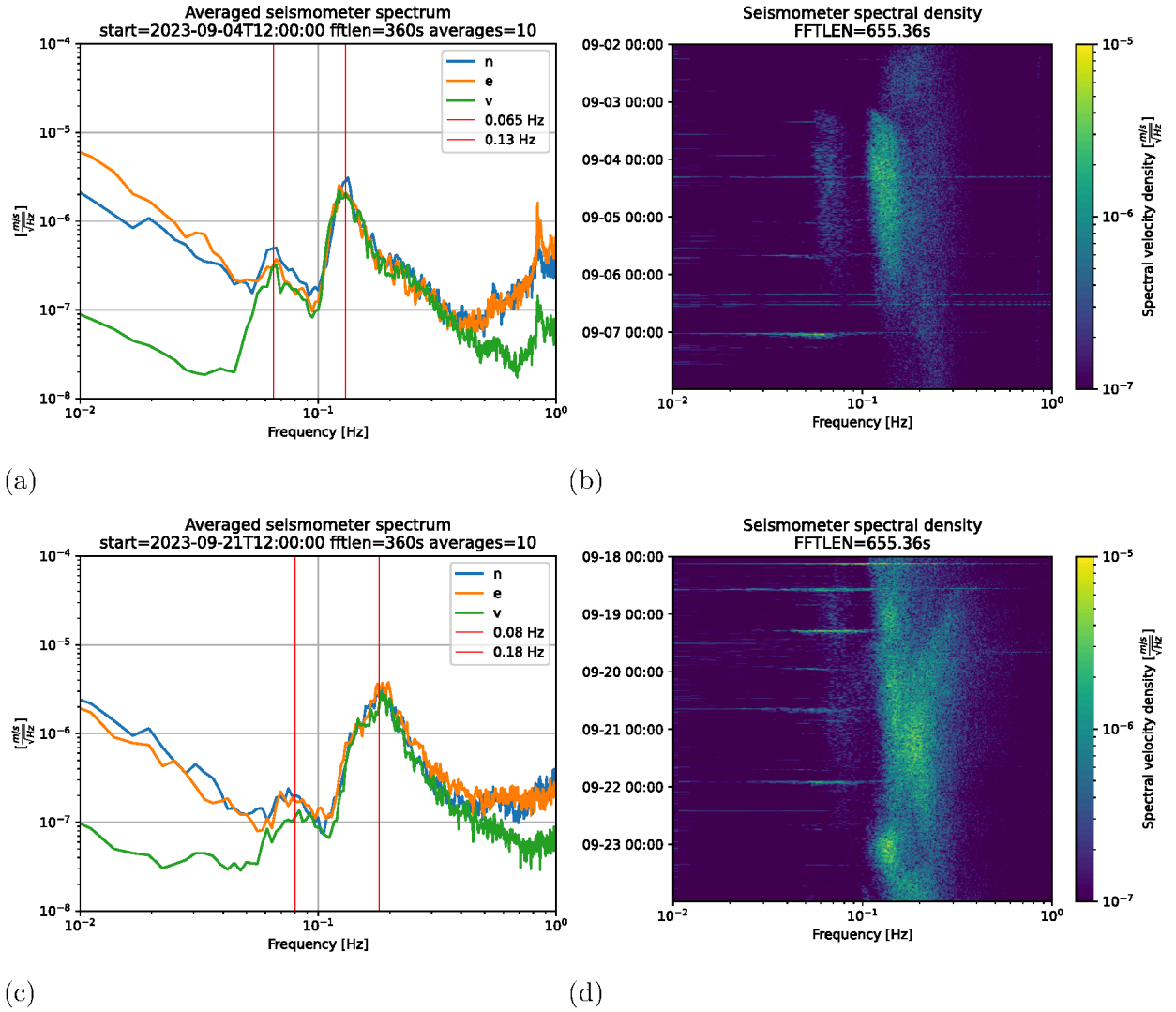
Figure 4.10: These figures show the seismometer data of the two periods in September with strong microseism: The days around the 4th and the 21st of September 2023. For each period there is one spectrogram of the vertical component, and an averaged spectral density of each component (north, east, vertical). The averaged spectral density is an average of ten periods in a total period of one hour.

Chapter 4.2 shows that the noise in the frequency range from 0.05 Hz to 0.5 Hz is of seismic origin. In this chapter, seismometer data is used, exploiting the three components (North, East, Vertical), to show the types of seismic waves and the mechanisms involved in their generation.

To get a nice, readable spectrum (Figure 4.10a and 4.10c) from the seismometer

measurements, some processing steps were performed. One hour of data, recorded at 200 Hz sample rate, was divided into 10 equally sized parts. The power spectral density was calculated for each part and finally averaged to a single power spectral density. Hanning window function was applied and the window size used for the discrete fourier transform (DFT) was 72000 Samples which corresponds to 360 s. This process was performed individually for each of the three components: north, east, and vertical. For more information on the measurement setup see Chapter 3.7.

The Figures 4.10a and 4.10c show a comparison of the three components of the seismometer: north, east, and vertical. Two distinct peaks can be seen in each spectrum: On the 4th of September (Figure 4.10a) at 0.065 Hz and 0.13 Hz. On 21st of September (Figure 4.10c) at 0.08 Hz and 0.17 Hz.

The two peaks could evolve from primary- (lower peak) and secondary (higher peak) ocean-generated microseism mechanisms. There are four observations that point in this direction. The fact that these peaks differ by almost exactly a factor of two (Chapter 2.2). The fact that the higher peak is much stronger than the lower peak. The fact that the clouds in the spectrogram around the given frequencies have a very similar shape and occur almost at the same time (Figure 4.10b). At the lower peak, the vertical component is much weaker than the horizontal components, while at the higher peak, the three components have the same amplitude. This was already observed by Becker et al. (2020) for primary and secondary microseism respectively.

As presented in Chapter 2.1, there are four main types of waves: primary, secondary, Love, and Rayleigh waves. Which types of waves are included in the ocean-generated microseism at the European XFEL? In general, ocean-generated microseism consists mainly of surface waves (Love and Rayleigh waves) (Juretzek & Hadziioannou 2016). Love and Rayleigh waves can be identified by comparing the ratio of vertical to horizontal components. While Rayleigh waves are expected to have equal amplitudes horizontally and vertically, Love waves have no vertical component at all (Figure 2.2). Figures 4.10a and 4.10c show that at the lower peaks (primary microseism) the vertical component is much weaker, suggesting a higher proportion of Love waves, while at the higher peak (secondary microseism) all three components have almost equal amplitudes, suggesting a high proportion of Rayleigh waves (Chapter 2.1).

4.4 Comparison with numerical ocean wave model Wavewatch III

The aim of this chapter is to find the origin of the ocean-generated microseism observed at the European XFEL. For this purpose, the seismometer measurements of Chapter 4.3 are compared with the ocean wave heights and periods in the North Sea and the North Atlantic, which are obtained from a sophisticated numerical model. Wavewatch III is a numerical model developed by the National Oceanic and Atmospheric Administration (NOAA) to forecast and calculate ocean waves (Tolman et al. 2009).

For this chapter, there are two important metrics: wave height and wave frequency.

Wave height refers to Significant Wave Height, which is the average height of the highest third of waves at a particular point in the ocean. Wave frequency refers to the inverse of the Peak Wave Period. The Peak Wave Period is the period of the most energetic waves passing through a particular point in the ocean. This corresponds to the group of waves that contribute the most energy. This results in a sudden jump each time a different group of waves becomes the strongest. Often these jumps represent swell fronts, but sometimes they are just artefacts of the ranking mechanism (Beccario 2015). All ocean wave frequencies and periods given below are taken from the Wavewatch III numerical model.

On 4 September 2023, strong ocean waves with heights of up to 7 metres and frequencies of around 0.08 Hz were present in the Azores. In the North Atlantic, near the Shetland Islands, strong ocean waves with significant wave heights of up to 5 metres and frequencies of around 0.07 Hz have been calculated. In the North Sea, ocean waves are much smaller, with significant wave heights below 1.5 metres and frequencies around 0.065 Hz. In the Baltic Sea, frequencies are around 0.25 Hz and significant wave heights are only around 0.5 metres. Therefore, no significant impact is expected from the Baltic Sea. The frequency of the primary microseism peak in the seismometer data matches very well with the frequencies of ocean waves in the North Atlantic near the Shetland Islands and the North Sea. It seems more likely that the primary microseism originates near the Shetland Islands, as the significant wave heights are much larger. In addition, the ocean waves are directed towards the Shetland Islands, and near the Shetland Islands there is a strong slope of the seabed from 200 metres down, whereas the North Sea is much shallower and has less slope. A sloping seabed is important for the generation of primary microseism as described in Ardhuin et al. (2015).

On 21 September 2023, at the location with the highest significant wave height of 7.5 metres in the North Atlantic, ocean wave frequencies are around 0.08 Hz. The same frequency dominates the North Sea but with smaller significant wave heights below 4 metres. These frequencies perfectly match the primary microseism peak in the seismometer data and would also explain the strong secondary microseism peak at 0.18 Hz. Only close to the coast are the ocean wave frequencies higher. In particular, in the German Bight with smaller significant wave heights below 2.5 metres, ocean waves have frequencies up to 0.3 Hz. It is possible that these ocean waves in the German Bight are visible on the seismometer data as local primary microseism and could explain the strong noise floor in Figure 4.10d at frequencies above the secondary microseism peak. Local primary microseism can only be observed close to the coast and the German Bight is only 100 km from the European XFEL and the seismometer. Local primary microseism is explained in detail in Becker et al. (2020).

In these two cases in September, the microseism peaks measured at the European XFEL correspond very well to the wave frequencies at the locations of the strongest ocean waves in the North Atlantic. However, it remains unclear from which of the two seas the microseism originated, as similar wave frequencies were present in the North Sea and the North Atlantic in the specific cases.

5 Discussion

This thesis demonstrates that ocean-generated microseism significantly impacts the bunch arrival time of the European XFEL in the frequency range of 0.05 to 0.5 Hz. Both primary and secondary ocean-generated microseism were identified using seismometers and a numerical reference model. Whereas secondary microseism has a strong impact on the bunch arrival time, primary microseism has no notable effect. This is attributed not only to the smaller amplitudes of secondary microseism but also to the fact that primary microseism has a higher Love wave to Rayleigh wave ratio. The effect on the bunch arrival time is caused by Rayleigh waves, whereas Love waves have a negligible influence on the bunch arrival time. In the presented cases, the noise originates from the North Atlantic and/or the North Sea. The amplitude of the noise depends on the weather conditions in the North Sea and the North Atlantic and is generally much stronger in winter. In summary, this study shows that ocean-generated microseism is a significant bottleneck that must be addressed to achieve femtosecond bunch arrival time stability.

An important aspect of this work is to prove that the noise observed at the European XFEL in the frequency range of 0.05 to 0.5 Hz is of seismic origin. Notably, the BAM and iDAS measurements correlate strongly, as shown in Chapter 4.2. Only downsampling and high-pass filtering of the iDAS signal are required to match the sampling frequency and remove temperature drifts. By using only a few simple signal processing methods, the analysis retains high significance and a low probability of error. Overall, the comparison shown in Chapter 4.2 proves that the given bunch arrival time jitter is caused by seismic activity, which must be addressed to achieve femtosecond bunch arrival time stability.

The correlation factor resulting from the regression is 88% higher than the expected factor from Formula 4.1. Apart from the scaling, the BAM data correlates strongly with the iDAS measurements, as shown in Figures 4.8 and 4.9. The discrepancy could be a factor of two, plus a further inaccuracy from, for example, the calibration factor of the iDAS. There are four main sources, this discrepancy could come from: The BAMs, the DAQ, the data processing performed for the comparison, and the calibration of the iDAS. The BAMs are listed here for completeness. Their calibration is important for the daily operation of the European XFEL and is therefore a very unlikely source of error. The DAQ is not the main source of BAM data for daily operations and is a complex system. Therefore, an error in this part of the chain is more likely. The analysis itself, including data processing, may be the source of error. Although the whole process from data retrieval to visualisation has been carefully checked, the possibility of a misunderstanding or a programming error remains. The last possible source is the calibration factor of the proprietary iDAS system provided by the manufacturer. It is difficult to check the calibration, due to the small magnitude of ocean-generated microseism, which is in the order of $1\,\frac{nm}{m}$. Notably, 10 m of single-mode fibre must be stretched exactly 10 nm with an

accuracy of at least 1 nm. In addition, the calibration is not important for most typical iDAS applications such as borehole or pipeline monitoring, geophysical exploration, and surveillance applications (Li et al. 2021). The evaluation of the calibration factor may be an interesting future study. The whole chain of BAM calibration, including data acquisition and data processing for comparison, can be checked by analysing a change in the bunch energy in front of the bunch compressors of the European XFEL. In such a case, the bunch arrival time changes by a known amount, which can be used as a reference to evaluate the whole BAM-related signal chain.

Earthquakes and urban car traffic can interfere with ocean-generated microseism. Earthquakes occur irregularly and last from minutes to hours. Measured amplitudes can be orders of magnitude larger than those of ocean-generated microseism. The frequency spectrum is typically very broad and can intersect with the ocean-generated microseism frequency range (Shearer 2019). Cars, however, only generate signals on channels in their immediate vicinity. Typically, some channels are stretched while others are compressed at the same time so that the sum of the car traffic signals over all channels is approximately zero (Figure 4.6). This makes it easy to remove car traffic from ocean-generated microseism, by calculating the average of multiple channels.

The identified primary and secondary microseism have a similar shape in the spectrogram (Figure 4.10b), suggesting that they originate from the same event, location, and time. The shape of the seismometer spectra agrees well with previous analyses reported by Shearer (2019), Becker et al. (2020), and Astiz (1997), where primary and secondary microseism peaks were observed at similar frequencies and amplitudes. There is also a similarity among their overall spectral shapes and in the ratios of vertical to horizontal components. Another shape is visible in Figure 4.10b at frequencies above 0.3 Hz, which has not been identified. This may be ocean-generated microseism from another event at another location, but it remains unclarified. Unfortunately, it is difficult to identify because it is overlapped by the strong secondary microseism.

The seismometer measurements show a strong secondary and a weak primary microseism peak, but in the BAM and iDAS measurements, only the secondary microseism peak is visible. One reason is that primary microseism is so weak that it is below or just above the noise floor in the BAM and iDAS measurements. In addition, primary microseism has a lower proportion of Rayleigh waves and a higher proportion of Love waves, as discussed in Chapter 4.3 and observed by Becker et al. (2020). Love waves induce only shear and no strain (Chapter 2.1). BAM and iDAS measurements only measure strain and cannot measure shear. Therefore, the influence of primary microseism on BAM and iDAS measurements is even smaller. As a result, not only is primary microseism not visible in BAM and iDAS measurements, but it does not have a significant effect on bunch arrival time jitter.

A limitation of this work is the small number of periods of strong ocean-generated microseism. For this work, data was collected from several instruments in September, and there were only two short periods with significant ocean-generated microseism. During one of the periods, the European XFEL was in tuning stage, which means that no BAM data is available for this event. In general, there are significantly more frequent and stronger periods of ocean-generated microseism in winter. Therefore, it is necessary to

perform measurements in winter to obtain more data and analyse stronger events.

6 Conclusion

This thesis demonstrates that ocean-generated microseism significantly impacts the bunch arrival time of the European XFEL within the frequency range of 0.05 to 0.5 Hz. The identification of both primary and secondary ocean-generated microseism using a seismometer and a numerical reference model reveals that while secondary microseism exerts a strong influence on the bunch arrival time, primary microseism has no notable effect. This difference can be attributed not only to the smaller amplitudes of primary microseism but also to its higher Love wave to Rayleigh wave ratio. Rayleigh waves are the main source of bunch arrival time jitter, whereas Love waves have a negligible influence. In the presented cases, the noise originates from the North Atlantic and/or the North Sea, and the amplitude of the noise is weather dependent, particularly stronger in winter. Generally, better bunch arrival time stability can be expected during summer.

The European XFEL enables cutting-edge precision in scientific experiments. To capture interactions of matter at the smallest scales, it is essential to manage any noise that influences the bunch arrival times. This work focuses on understanding the relevance of ocean-generated microseism and its impact on experiments. In conclusion, this study shows that ocean-generated microseism is a significant bottleneck that must be addressed to achieve femtosecond bunch arrival time stability.

7 Acknowledgements

The work presented in this thesis has been supported by several other people. First of all, I would like to thank my supervisor, Dr. Holger Schlarb. I was always given the freedom to go into any research direction and to explore my ideas without limitations. Our numerous and long discussions were very valuable and allowed me to keep a critical view of the new field of research I have explored in this dissertation. I would also like to thank my supervisor Prof. Dr. Carsten Burmeister for his support throughout the writing process. I was lucky to work with great colleagues who supported me and introduced me to the new research areas. My thanks go to my colleague Dr. Markus Hoffmann, with whom I have pursued many exciting projects. To Prof. Dr. Celine Hadziioannou for her insights into geophysics and ocean-generated microseisms. I am grateful for the introduction to the relevant parts of the European XFEL and accelerator physics in general by Dr. Marie Czwalinna. I would also like to thank Prof. Dr. Oliver Gerberding from the University of Hamburg for providing the iDAS interrogator, without which this project would not have been possible. And to Norbert Meyners and Iris Gehrmann for providing the seismometer data. Finally, I would like to thank Prof. Dr. Volker Gülzow for suggesting that I take part in this project and for his constant support.

Bibliography

Agababyan, A., Asova, G., Dimitrov, G., Grygiel, G., Fominykh, B., Hensler, O., Kammering, R., Petrosyan, L., Rehlich, K., Rybnikov, V. et al. (2007), Multi-processor based fast data acquisition for a free electron laser and experiments, *in* '2007 15th IEEE-NPSS Real-Time Conference', IEEE, pp. 1–5.

Altarelli, M. et al. (2006), 'XFEL: The European X-Ray Free-Electron Laser - Technical Design Report', pp. 1–646.
URL: *https://bib-pubdb1.desy.de/record/77248*

Anderson, D. N., Fagan, D. K., Tinker, M. A., Kraft, G. D. & Hutchenson, K. D. (2007), 'A mathematical statistics formulation of the teleseismic explosion identification problem with multiple discriminants', *Bulletin of the Seismological Society of America* **97**(5), 1730–1741.

Angelovski, A., Kuhl, A., Hansli, M., Penirschke, A., Schnepp, S. M., Bousonville, M., Schlarb, H., Bock, M. K., Weiland, T. & Jakoby, R. (2012), 'High bandwidth pickup design for bunch arrival-time monitors for free-electron laser', *Physical Review Special Topics-Accelerators and Beams* **15**(11), 112803.

Angelovski, A., Kuntzsch, M., Czwalinna, M. K., Penirschke, A., Hansli, M., Sydlo, C., Arsov, V., Hunziker, S., Schlarb, H., Gensch, M., Schlott, V., Weiland, T. & Jakoby, R. (2015), 'Evaluation of the cone-shaped pickup performance for low charge sub-10 fs arrival-time measurements at free electron laser facilities', *Phys. Rev. ST Accel. Beams* **18**, 012801.
URL: *https://link.aps.org/doi/10.1103/PhysRevSTAB.18.012801*

Ardhuin, F., Gualtieri, L. & Stutzmann, E. (2015), 'How ocean waves rock the earth: Two mechanisms explain microseisms with periods 3 to 300 s', *Geophysical Research Letters* **42**(3), 765–772.

Astiz, L. (1997), Characteristic low and high noise models from robust pse of seismic noise of broadband stations, *in* 'IASPEI 1997 meeting'.

Beccario, C. (2015), 'earth'.
URL: *https://github.com/cambecc/earth*

Becker, D., Cristiano, L., Peikert, J., Kruse, T., Dethof, F., Hadziioannou, C. & Meier, T. (2020), 'Temporal modulation of the local microseism in the north sea', *Journal of Geophysical Research: Solid Earth* **125**(10), e2020JB019770.

Bi, F., Song, J., Wu, K. & Xu, Y. (2015), 'Evaluation of the simulation capability of the wavewatch iii model for pacific ocean wave', *Acta Oceanologica Sinica* **34**, 43–57.

Bock, M. K. (2013), 'Measuring the electron bunch timing with femtosecond resolution at flash'.

Bretschneider, C. L. (1959), *Wave variability and wave spectra for wind-generated gravity waves*, number 118, The Board.

Chen, Y.-N., Gung, Y., You, S.-H., Hung, S.-H., Chiao, L.-Y., Huang, T.-Y., Chen, Y.-L., Liang, W.-T. & Jan, S. (2011), 'Characteristics of short period secondary microseisms (spsm) in taiwan: The influence of shallow ocean strait on spsm', *Geophysical Research Letters* **38**(4).

Czwalinna, M., Kral, J., Lautenschlager, B., Mueller, J., Schlarb, H., Schulz, S., Steffen, B., Boll, R., Kirkwood, H., Koliyadu, J. et al. (2021), 'Beam arrival stability at the european xfel', *Proc. IPAC 2021* pp. 3714–3719.

Decking, W., Abeghyan, S., Abramian, P., Abramsky, A., Aguirre, A., Albrecht, C., Alou, P., Altarelli, M., Altmann, P., Amyan, K. et al. (2020), 'A mhz-repetition-rate hard x-ray free-electron laser driven by a superconducting linear accelerator', *Nature photonics* **14**(6), 391–397.

DESY (2023), 'European xfel'.
  URL: *https://www.desy.de/research/facilities_projects/european_xfel/index_eng.html*

Dinter, H. (2018), Longitudinal diagnostics for beam-based intra bunch-train feedback at FLASH and the European XFEL, PhD thesis, Staats-und Universitätsbibliothek Hamburg Carl von Ossietzky.

Dinter, H., Czwalinna, M., Gerth, C., Przygoda, K., Rybaniec, R., Schlarb, H., Sydlo, C. et al. (2015), 'Prototype of the improved electro-optical unit for the bunch arrival time monitors at flash and the european xfel', *TUP049, FEL* **15**.

Elleaume, P., Chavanne, J. & Faatz, B. (2000), 'Design considerations for a 1 å sase undulator', *Nuclear Instruments and Methods in Physics Research Section A: Accelerators, Spectrometers, Detectors and Associated Equipment* **455**(3), 503–523.

Fuhrmann, P. & Gülzow, V. (2006), dcache, storage system for the future, *in* 'Euro-Par 2006 Parallel Processing: 12th International Euro-Par Conference, Dresden, Germany, August 28–September 1, 2006. Proceedings 12', Springer, pp. 1106–1113.

Geloni, G., Saldin, E., Samoylova, L., Schneidmiller, E., Sinn, H., Tschentscher, T. & Yurkov, M. (2010), 'Coherence properties of the european xfel', *New Journal of Physics* **12**(3), 035021.

Guy, M. R., Patton, J. M., Fee, J., Hearne, M., Martinez, E., Ketchum, D., Worden, C., Quitoriano, V., Hunter, E., Smoczyk, G. et al. (2015), National earthquake information center systems overview and integration, Technical report, US Geological Survey.

Gü (2019), *Test And Calibration data, CMG-3TD.*

H. Schlarb, M.K. Czwalinna, S. S. (2023), Femtosecond synchronization of large scale fels - achievements, limitations and mitigation paths, *in* 'FLS2023 - Proceedings - Luzern, Switzerland'.
URL: *https://fls2023.vrws.de/talks/we3d1_talk.pdf*

Hadziioannou, C. & Gerberding, O. (2023), 'Wave initiative hamburg'.
URL: *http://wave-hamburg.eu/*

Hartog, A. H. (2017), *An introduction to distributed optical fibre sensors*, CRC press.

Juretzek, C. & Hadziioannou, C. (2016), 'Where do ocean microseisms come from? a study of love-to-rayleigh wave ratios', *Journal of Geophysical Research: Solid Earth* **121**(9), 6741–6756.

Kirkwood, H. J., Letrun, R., Tanikawa, T., Liu, J., Nakatsutsumi, M., Emons, M., Jezynski, T., Palmer, G., Lederer, M., Bean, R. et al. (2019), 'Initial observations of the femtosecond timing jitter at the european xfel', *Optics letters* **44**(7), 1650–1653.

Li, Y., Karrenbach, M. & Ajo-Franklin, J. (2022), *Distributed acoustic sensing in geophysics: Methods and applications*, Vol. 268, John Wiley & Sons.

Li, Y., Karrenbach, M. & Ajo-Franklin, J. B. (2021), 'A literature review: Distributed acoustic sensing (das) geophysical applications over the past 20 years', *Distributed Acoustic Sensing in Geophysics: Methods and Applications* pp. 229–291.

Löhl, F. (2009), 'Optical synchronization of a free-electron laser with femtosecond precision'.

Longuet-Higgins, M. S. (1950), 'A theory of the origin of microseisms', *Philosophical Transactions of the Royal Society of London. Series A, Mathematical and Physical Sciences* **243**(857), 1–35.

Meteostat (2024), 'Helgoland wind plot', https://meteostat.net/en/place/de/helgoland?s=10015&t=20 01-05/2024-01-12. Accessed: January 12, 2024.
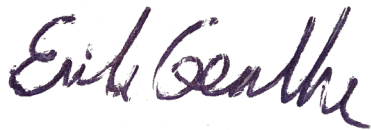**URL:** *https://meteostat.net/en/place/de/helgoland?s=10015&t=2024-01-05/2024-01-12*

Naldrett, G., Cerrahoglu, C. & Mahue, V. (2018), 'Production monitoring using next-generation distributed sensing systems', *Petrophysics* **59**(04), 496–510.

Nishida, K., Kawakatsu, H., Fukao, Y. & Obara, K. (2008), 'Background love and rayleigh waves simultaneously generated at the pacific ocean floors', *Geophysical Research Letters* **35**(16).

Palmer, G., Kellert, M., Wang, J., Emons, M., Wegner, U., Kane, D., Pallas, F., Jezynski, T., Venkatesan, S., Rompotis, D., Brambrink, E., Monoszlai, B., Jiang, M., Meier, J., Kruse, K., Pergament, M. & Lederer, M. J. (2019), 'Pump–probe laser system at the FXE and SPB/SFX instruments of the European X-ray Free-Electron Laser Facility', *Journal of Synchrotron Radiation* **26**(2), 328–332.
URL: *https://doi.org/10.1107/S160057751900095X*

Parker, T., Shatalin, S. & Farhadiroushan, M. (2014), 'Distributed acoustic sensing–a new tool for seismic applications', *first break* **32**(2).

Rathje, E. M., Abrahamson, N. A. & Bray, J. D. (1998), 'Simplified frequency content estimates of earthquake ground motions', *Journal of geotechnical and geoenvironmental engineering* **124**(2), 150–159.

Schulz, S., Czwalinna, M., Felber, M., Fenner, M., Gerth, C., Kozak, T., Lamb, T., Lautenschlager, B., Ludwig, F., Mavric, U. et al. (2019), Few-femtosecond facility-wide synchronization of the european xfel, *in* 'Proceedings of the 39 the International Free-Electron Laser Conference (Hamburg)'.

Shearer, P. M. (2019), *Introduction to seismology*, Cambridge university press.

Tolman, H. L. et al. (2009), 'User manual and system documentation of wavewatch iii tm version 3.14', *Technical note, MMAB Contribution* **276**(220).

Eidesstattliche Erklärung

Ich erkläre hiermit an Eides statt, dass ich die vorliegende Arbeit selbstständig und ohne Benutzung anderer als der angegebenen Hilfsmittel angefertigt habe; die aus fremden Quellen direkt oder indirekt übernommenen Gedanken sind als solche kenntlich gemacht. Die Arbeit wurde bisher in ähnlicher Form keiner anderen Prüfungskommission vorgelegt und auch nicht veröffentlicht.

Erik Genthe, Hamburg, 16.2.2023